8-1-2012

Magnetic Properties Study of the Mn-Al System with Additions of B or C and Mechanical Milling Techniques

Timothy E. Prost
University of Nebraska-Lincoln, tmthprost2@gmail.com

MAGNETIC PROPERTIES STUDY OF THE Mn-Al SYSTEM WITH ADDITIONS OF B OR C AND MECHANICAL MILLING TECHNIQUES

By

Timothy E. Prost

A THESIS

Presented to the Faculty of

The Graduate College at the University of Nebraska

In Partial Fulfillment of Requirements

For the Degree of Master of Science

Major: Engineering Mechanics

Under the Supervision of Professor Jeffrey E. Shield

Lincoln, Nebraska

August, 2012

MAGNETIC PROPERTIES STUDY OF THE Mn-Al SYSTEM

WITH ADDITIONS OF B OR C AND MECHANICAL MILLING TECHNIQUES

Timothy E. Prost, M.S.

University of Nebraska, 2012

Adviser: Jeffrey E. Shield

Recently a shift in the focus of permanent magnetic research has moved from Rare Earth (RE)-based alloys to those made from more readily available elements. Because of their relatively large magnetocrystalline anisotropy, $L1_0$ compounds have the potential for use as permanent magnet materials. One particular alloy that is readily available and inexpensive is near equi-atomic manganese and aluminum (Mn_{50}-Al_{50}). First characterized in 1958, it did not receive much attention until more recently when RE supply chain issues made the alloy more attractive for commercial and research applications. The ferromagnetic (FM) τ-phase ($L1_0$) is metastable and formed from a parent, high-temperature ε-phase (A3). The ε-phase can be retained at room temperature by rapid quenching, and subsequent annealing transforms it to the τ-phase. For this reason the stability of both phases has been explored and the addition of carbon has been noted to improve stability.

This study explores a number of alloying and processing schemes designed to improve the magnetic properties. These include the effect of boron additions, and novel mechanical milling techniques. Manganese-aluminum permanent magnets were synthesized by arc-melting and subsequent melt-spinning with different alloy compositions. The magnetic properties, X-ray diffraction patterns, and the phase

transformation kinetics were analyzed. Boron is found to have little to no effect on the formation of the FM τ-phase ($L1_0$) or its parent ε- phase (A3) and in fact reduces the stability of the metastable phases in favor of the equilibrium phases (βMn (A13) and γ_2 ($D8_{10}$)), resulting in an overall deleterious effect on magnetic performance. Post-processing techniques such as High Energy Ball Milling (HEBM) and Surfactant Assisted Mechanical Milling (SAMM) were determined to increase the coercivities of the alloys. Maximum coercivities (H_c) of 3.88 kOe and 4.22 kOe were observed for the HEBM samples and SAMM samples, respectively. Furthermore a maximum saturation magnetization (M_s) of 134 emu/g was measured for a ternary alloy of $Mn_{54}Al_{44}C_2$ which is the highest reported.

AUTHOR'S ACKNOWLEDGEMENTS

First I would like to express my appreciation to Dr. Jeff Shield, my adviser, for being a major influence and for helping me enjoy my time in his group. I would also like to thank everyone else in our group for their help throughout my time here; and thanks to the NCMN faculty and staff (as well as the students) who helped with experiments and allowed me to use their equipment.

I would like to thank the rest of my committee: Dr. Mehrdad Negahban, the driving force behind the EMME program, without whom it would not exist; Dr. Jean-Marc Saiter, who always treated me as an equal and graciously opened the doors of the LECAP to us; and Dr. Jean-Marie LeBreton, for guiding my research and teaching me (often in English) the fundamentals of magnetism in his spare time.

I thank my family and friends, who have been behind me throughout my academic career, especially my parents to whom I owe everything. And of course, thank you Sarah for always being there for me and helping me along the way.

GRANT INFORMATION

I would like to thank the Department of Energy, specifically the Advanced Research Projects Agency – Energy department who funded my research at UNL through the REACT project (DE-AR0000186). I would also like to acknowledge and thank the U.S. Department of Education for funding through the FIPSE-ATLANTIS grant (P116J070028) and the European Union Erasmus Mundus program for funding my travel and studies abroad at the Université de Rouen, France.

CONTENTS

LIST OF FIGURES

Chapter 1

INTRODUCTION

Magnetic materials have many important applications in energy production and utilization as well as numerous information science applications ranging from small, precise actuator motors to electronic storage media. The basic principles of magnetism can be explained by first explaining the different types of magnetism. The fundamental properties of magnetism arise from unpaired inner shell electrons which have an intrinsic spin. This spin gives rise to an individual magnetic moment attributed to each atom with these unpaired electrons.

1.1Magnetism

There are a few different common types of magnetic materials: ferromagnetic (FM), ferrimagnetic, antiferromagnetic (AF), paramagnetic (PM), and superparamagnetic (SP) (Figure 1). Ferromagnetism is characterized by a parallel alignment of individual atom's magnetic moments. Ferrimagnetism is similar to ferromagnetism; however there is antiparallel coupling between atoms with or groups a large magnetic moment and smaller ones which leads to a net magnetization for the material. It should be noted that this is most commonly found in compounds like magnetite ("lode stone", Fe_3O_4). AF materials exhibit the same antiparallel coupling of magnetic moments but the net moment is zero for the bulk material because each couple has an equal but opposite magnetic moment. PM materials are similar to AF in that there is no net magnetic moment; however the

mechanism for this is different. PM materials have randomly oriented moments, and FM materials will become PM at the Curie temperature (T_c) where the magnetism drops drastically as a result. SP material characteristics will be discussed later in the introduction.

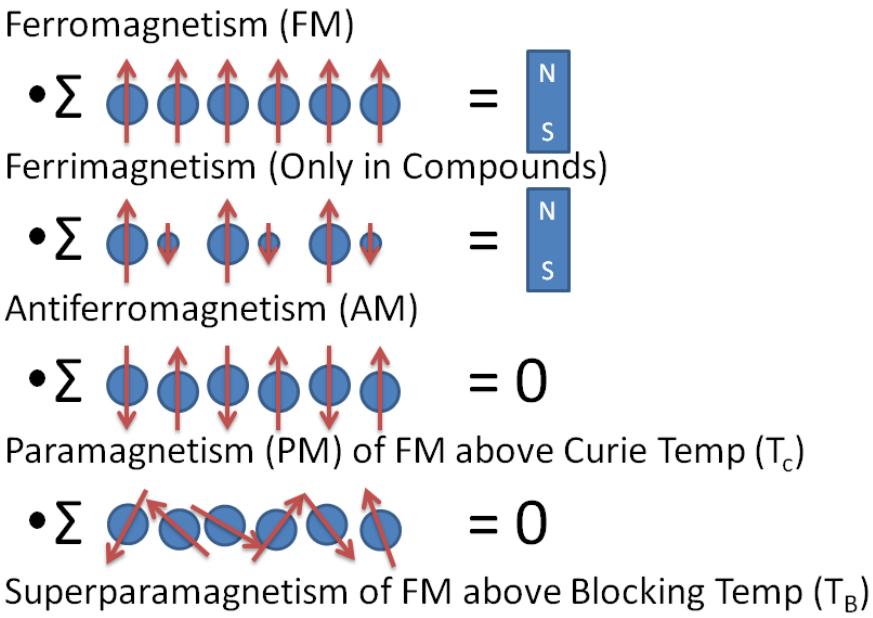

Figure 1 Depiction of various types of magnetism and some extra information.

For this study, knowledge of FM materials' reaction to external magnetic fields is necessary. When FM materials are exposed to a magnetic field they exhibit hysteresis with their internal magnetism, which can be seen in Figure 2. As a FM material is exposed to an external "applied" magnetic field (H) the internal magnetism (B or M) will increase from the origin to a and up to B_s which is the saturation in Gauss (G). The relation between B and M is

$$B = H + 4\pi M, \qquad (1)$$

and the units for each are equivalent (1G = 1emu). A review of the units commonly used in magnetism is listed in Table 1 with conversions from cgs to mks(SI) units even though throughout the literature they are used almost interchangeably.

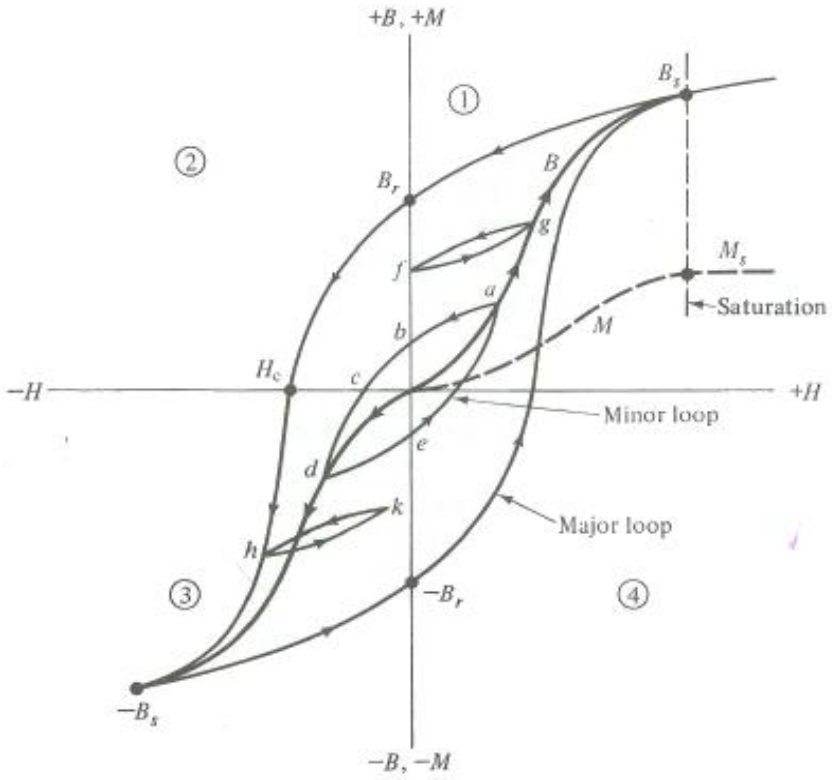

Figure 2 Typical Ferromagnetic (FM) Hysteresis Curve [1]

Table 1 Review of typical units used in magnetism[1].

Quantity	Symbol	Gaussian and cgs units	Conversion	SI (mks) units
Magnetic Induction	B	Gauss (G)	10^{-4}	Tesla (T), Wb/m^2
Magnetic Field	H	Oersted (Oe), Gb/cm	$10/4\pi$	A/m
Volume magnetization	M	emu/cm^3	10^3	A/m
Volume magnetization	$4\pi M$	G	$10^3/4\pi$	A/m
Mass magnetization	σ, M	emu/g	1 $4\pi \cdot 10^{-7}$	$A \cdot m^2/kg$ $Wb \cdot m/kg$

Once saturation (B_s or M_s) is achieved, the applied field (H) is reduced to zero, at which point there is a magnetization that remains in the material (remanence magnetism, B_r). The direction of the applied field is then reversed and the curve continues down to the point labeled H_c (sometimes iH_c or H_{ci}). The magnitude of H at this point is the coercivity (sometimes called the coercive force or coercive field), a quantity related to the strength of the permanent magnet. The coercivity is a measure of how much applied field it takes to reduce the internal magnetization of the material to zero. It is important to note that the field measured at this point on a B(H) curve in Figure 2 is actually ${}_BH_c$ and H_c is measured from a M(H) curve. At this point, the field is increased in the negative direction until saturation is reached again. If saturation is not reached before the magnetic field is reversed, then a minor loop is made ($abcde$) in Figure 2 instead of a major loop. The magnetic properties (B_s, B_r, H_c) cannot be determined from a minor loop. However, a technique called the approach to saturation can be used to determine the saturation value of a sample if the measurement is sufficiently close to the saturating field in any direction; this field specifically in the hard magnetic direction is called the anisotropy field (H_A or H_K), given by

$$H_A = 2K_1/M_s, \tag{2}$$

where K_1 is the first anisotropy constant in ergs/cm^3, and M_s is the saturation magnetization in emu/cm^3 [1]. If this requirement is satisfied, then the approach to saturation fit (Equation (3)) can be used to approximate M_s.

$$M = M_s\left(1 - \frac{a}{H} - \frac{b}{H^2}\right), \tag{3}$$

where a and b are empirical values to be calculated.

Permanent magnets are magnets that are by name permanent, but more practically they are magnets with large coercivity and exhibit a rather “square” hysteresis loop. The ratio between saturation and remanent magnetization (B_r/B_s or M_r/M_s) is sometimes reported as the squareness ratio and a value closer to 1 is usually preferable for practical permanent magnets.

As with any metal, FM metals are comprised of many grains, each of which are comprised of a single contiguous crystal structure (however, defects are usually prevalent). When the FM material is magnetized each grain will have a preferred direction in which to magnetize, but not all of an individual grain will agree and may form multiple magnetic domains. Each of these domains can grow and combine to give the whole grain a uniform magnetization (saturation) and all of the domains in a FM tend to interact with other nearby domains. These interactions are called magnetostatic interactions, and will cause the coercivity of a material to decrease through a cascade effect. The best way to avoid this effect is to reduce the grain size until it reaches a size that can support only a single domain. Another way is to impede the movement of the domain walls using defects or secondary phases.

When a particle of FM material approaches the single magnetic domain range, a drastic increase in the intrinsic coercivity (H_{ci}) is observed in some materials, as can be seen in Figure 3 (1 to 2 orders of magnitude). It is clear that a ten-fold increase in H_{ci} is possible for these materials. A diagram of the characteristic curve and its meaning is present in Figure 4 where at large particle size there exist multiple domains (MD) within each particle. However, in the case of soft magnetic materials, once the particle size

approaches the critical particle diameter for single domain transition (D_s) the coercivity begins to increase until the size reaches D_s. For hard magnetic materials, the D_s is typically on the scale of 100nm; however, further increase in H_{ci} (or magnetic hardening) can be seen below this limit and following a similar trend as in Figure 4. Below this maximum the H_{ci} decreases as the domains begin to decrease in size with the particles/grains until a point when the material exhibits SP tendencies which results in the decrease of the H_{ci} to zero. FM materials will exhibit SP behavior above the blocking temperature (usually below room temperature (RT) for very small particles). This temperature can be determined from the Neel-Brown expression,

$$\tau = \tau_0 exp\left(\frac{KV}{kT_B}\right) \quad (4)$$

where τ is the relaxation time, τ_0 is the characteristic time of the system taking the measurement, K is the anisotropy constant, V is the volume of the particle, and k is the Boltzmann constant. T_B is the temperature below which the particles become "blocked", meaning it will not randomly flip due to thermal effects, and will exhibit FM characteristics. The critical diameter D_s is calculated from (4) by determining V for room or operating temperature of the magnet and assuming a spherical particle. Therefore for permanent magnet applications where the size needs to be small and the maximum operating temperature is fixed, there exists a minimum size to which the particles can be reduced. This is particularly problematic for recording media such as computer hard drives where the goal is to fit as much data onto as small of an area as possible.

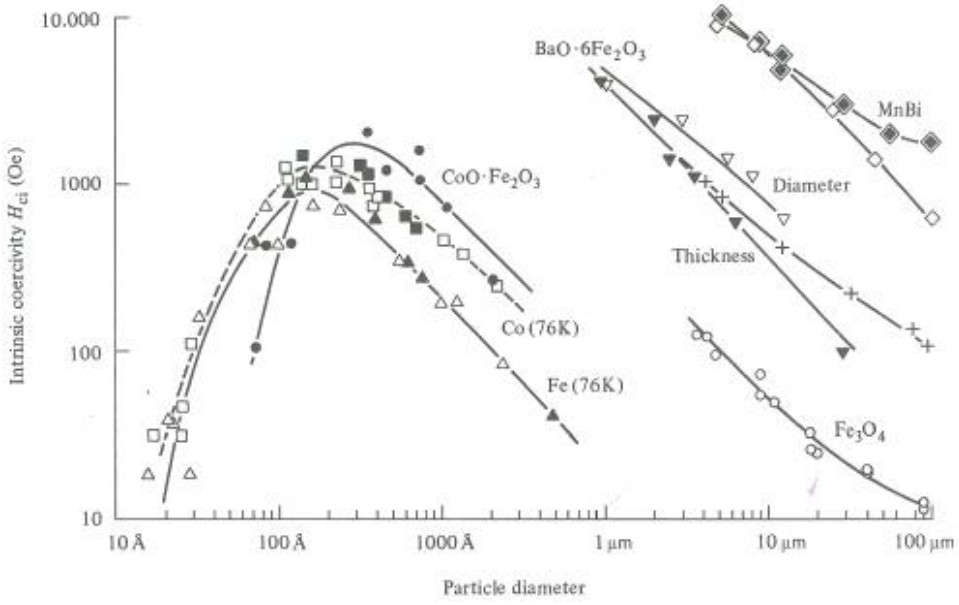

Figure 3 Experimental data of particle size vs. intrinsic coercivity, Hci (Oe)[1]. Note examples include soft magnetic materials only.

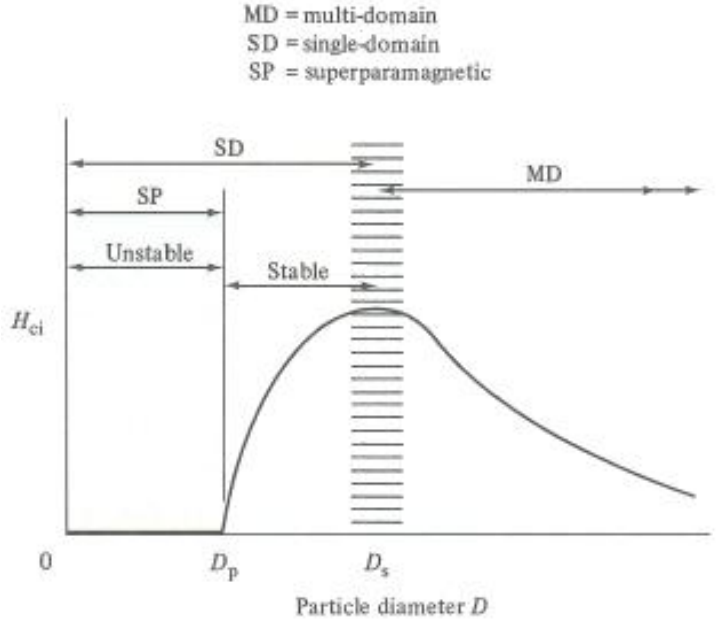

Figure 4 Depiction of characteristic increase in Hci vs. particle size with regions labeled[1]. SD and MD regions will depend on microstructure and be different for hard and soft magnetic materials.

Also, it has been noted in [2] that while decreasing particle size, some of the particles may begin to exhibit superparamagnetic behavior that influences the slope at high field. If this is the case, the law of approach to saturation will not fit well with the experimental data and an additional term to address this has been suggested by [2]. Making the proposed law of approach to saturation for a mix of FM and SP particles,

$$M = M_{s,f}\left(1 - \frac{a}{H} - \frac{b}{H^2}\right) + M_{s,sp}\left(\coth\alpha - \frac{1}{\alpha}\right) \quad (5)$$

where $M_{s,f}$ and $M_{s,sp}$ are the FM and SP phases saturation magnetization, respectively; $L(\alpha) = \coth(\alpha) - 1/\alpha$ is the Langevin function describing SP behavior where $\alpha = \mu_{eff}H/k_BT$; $\mu_{eff} = M_s\langle V\rangle$ is the effective magnetic moment; and $\langle V\rangle$ is the volume fraction of the SP particles. It was concluded that this approach is a good fit and can elucidate the magnetization process for the melt-spun Fe-Cu granular system [2].

1.2Phase Transformations

Another crucial aspect of this study is phase transformations in metals because having the correct crystalline structure will give the metal its magnetic properties. The change in crystalline structure follows one of two methods, diffusion or diffusionless, for all phase transformations. Diffusion-driven transformations require a substantial amount of energy to physically move atoms around, and this energy is usually provided through thermal energy. The random kinetic energy of each individual atom, based upon its temperature, is what drives the diffusion process in most phase transformations. Other methods of phase transformation include mechanical deformation but this usually induces an increase in the temperature of the material as well.

Typically phase diagrams are created one composition at a time. An individual sample is placed in a furnace and heated to its melting point while the heat flow to the sample or the specific energy of the sample is measured compared to a reference sample that is heated at the same time. In this way the phase lines for a phase diagram can be created. This process is outlined below in Figure 5 starting from a, where the specific heat vs. temperature was measured for each composition with the arrows marking appearance and disappearance of excess specific heat that correspond to the up and down black triangles (▲and▼) in Figure 5 c. The increase and decrease of heat of absorption in Figure 5 b suggest the eutectoid reactions at points E and H (Figure 5 b and c). Also, phase transformations can be measured with a differential thermal analyzer (DTA) which measures only the heat flow to or from a sample compared to a reference sample. The method with which to create a phase diagram is similar to that outlined above, however less accurate due to sometimes large experimental error.

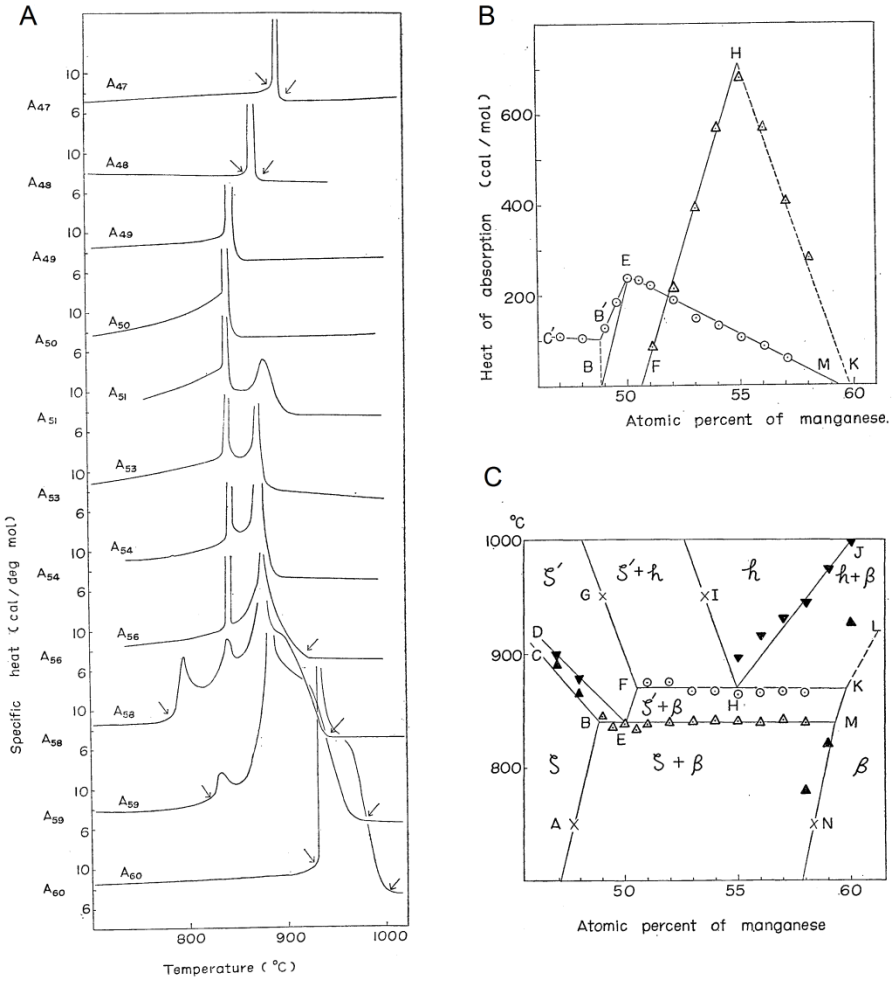

Figure 5 Process for creating a phase diagram. a.) specific heat vs. temperature to determine changes in structure b.) adiabatic measurements of heat of absorption vs. composition c.) created phase diagram from A and B[3].

1.3Motivation

Recently there has been a shift in permanent magnet research from the strong and recently supply limited rare earth (RE) based magnets to those based upon more inexpensive materials. The problem is however, while these materials create a less expensive magnet; they are on average much weaker than Nd-Fe-B magnets (highest reported energy product). Research and development has progressed nonetheless due to a recent, drastic increase in the price of RE metals. If these materials can begin to fill the void between ferrite magnets and RE permanent magnets, then they can be an economic replacement for many low energy systems. Currently, the vast majority of the world supply of RE elements rest in China (as well as the largest deposits of the ore from which RE elements are mined), and unless mining restrictions are lifted or relaxed in the U.S., China will continue to control the market. The world supply can be seen in Figure 6, with China supplying more than 90% of the U.S. market.

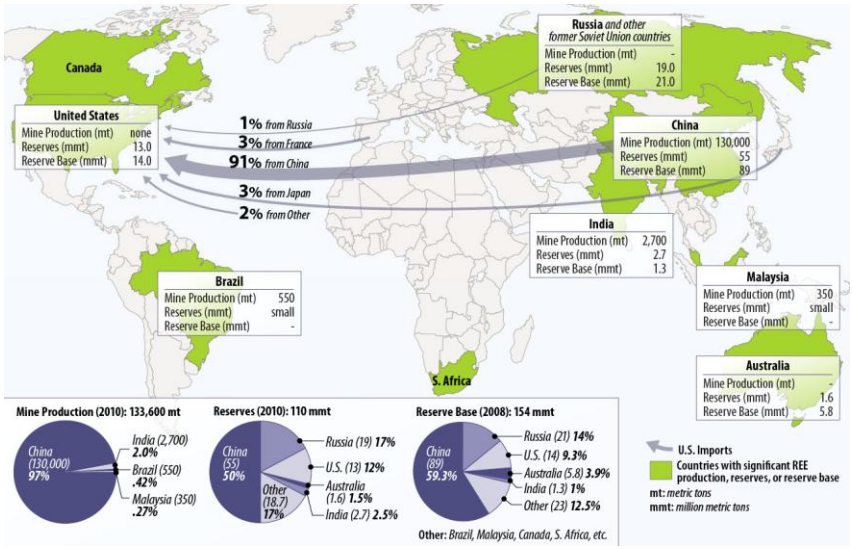

Figure 6 U.S. Geological Survey, Mineral Commodity Summaries, 2008-2011 (Figure created by CRS)

Also, it is interesting to notice the increase in the rest of world (ROW) demand when compared to the increase of Chinese demand of RE elements. As can be seen in Figure 7, the increase of the world supply and demand is coupled with the increase of the Chinese involvement in the market.

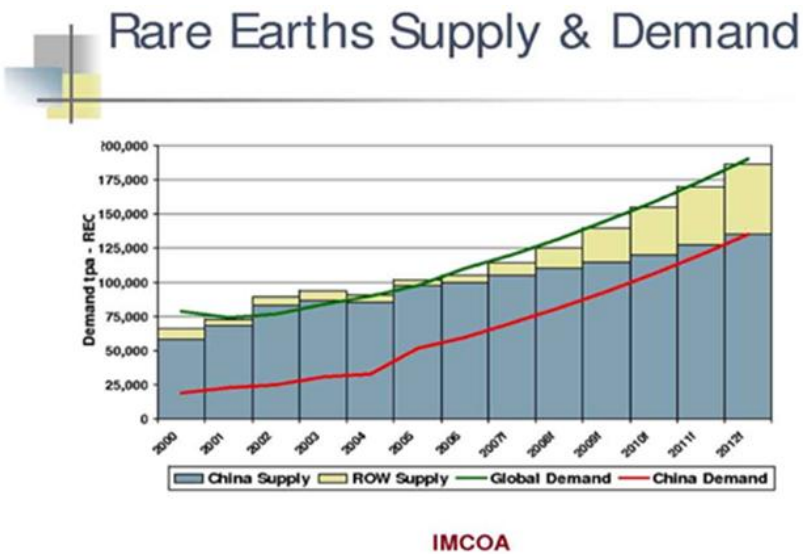

Figure 7 RE Supply and Demand (Courtesy of GWG and Dudley Kingsnord)

It is estimated that the growth of Chinese supply will be equaled by its demand in the near future leaving the ROW without RE elements. This is an increasing and dangerous problem as the majority of modern technology depends on magnets of some kind, and highly efficient electricity production requires very strong permanent magnets. Therefore, the search for more inexpensive replacements has been a goal for the science community as a whole and more specifically the U.S. Department of Energy (DOE), which has funded this study. Although the outlook for creating a non-RE magnet with the same properties of NdFeB magnets is bleak, there is a niche that can be filled with more inexpensive magnets made without importing expensive RE elements.

1.4Literature Review

The focus of this study is on the ordered face centered tetragonal (fct) $L1_0$ crystalline structure (Figure 9 b) and therefore it is necessary to see what else has been done in similar systems. Attempts have been made with alloys such as Fe-Pt, and Pt-Co, also calculations have been done on the systems following the trend MT (M= Rh,Pd,Ir,Pt; and T= Mn, Fe, Co, Ni) [4]. However, many of these metals are as expensive as or more expensive than RE metals (e.g. Pt) and with commercial applications, cost is always a motivating factor. Fe-Pd L10 alloys have been extensively explored by Klemmer et. al. and promising mechanisms for coercivity enhancement have been suggested. However, the overall adjustment in coercivity was on the order of 500 Oe (from 350 to 800 Oe) for this particular alloy, meaning it is not fit for permanent magnet applications [5].

The FM $L1_0$ manganese-aluminum alloy has been known and characterized since the late 1950's [3,6], but research on this alloy was not thoroughly conducted until more recently. With the help of some more modern processing and characterization techniques, the FM Mn-Al phase can be fabricated on an industrial level for commercial and research applications. Also, more recently a FM α-Mn-type Mn-Al alloy has been discovered, however its magnetic properties are inferior to those of the $L1_0$ FM alloy (M_s = 11 emu/g)[7].

The FM phase in the Mn-Al system (referred to as the τ-phase) was first characterized thermodynamically in 1958 by Kono [3] along with its structure, morphology, and magnetic properties and stabilizing additions of carbon were explored by Koch et. al. [6] only two years later. The phase diagram for this system has since been completed and is

shown in Figure 8 with the ε-phase in the range of 53 to 60 at% Mn. The difficulty lies in achieving this phase. Because it is a high temperature phase, it must be formed from non-equilibrium processing techniques. This method of processing hinges on the formation of the ε-phase because it is a parent phase to the magnetic $L1_0$ τ-phase. The formation of the ε-phase (hcp, Figure 9 a) is achieved by rapid quenching techniques, such as melt-spinning[8], but can be done by other processes[9,10,11,12,13,14,15,16,17,18] mostly involving water quenching, but in one case[9] involving something called splat quenching. The rapid cooling process not only provides sufficient undercooling for the room temperature stability of the disordered ε (hcp) phase, but it also keeps the grain size small and introduces defects to the microstructure. The τ-phase is formed in the two-phase region consisting of γ_2 and βMn (dashed lines in Figure 8) and is metastable.

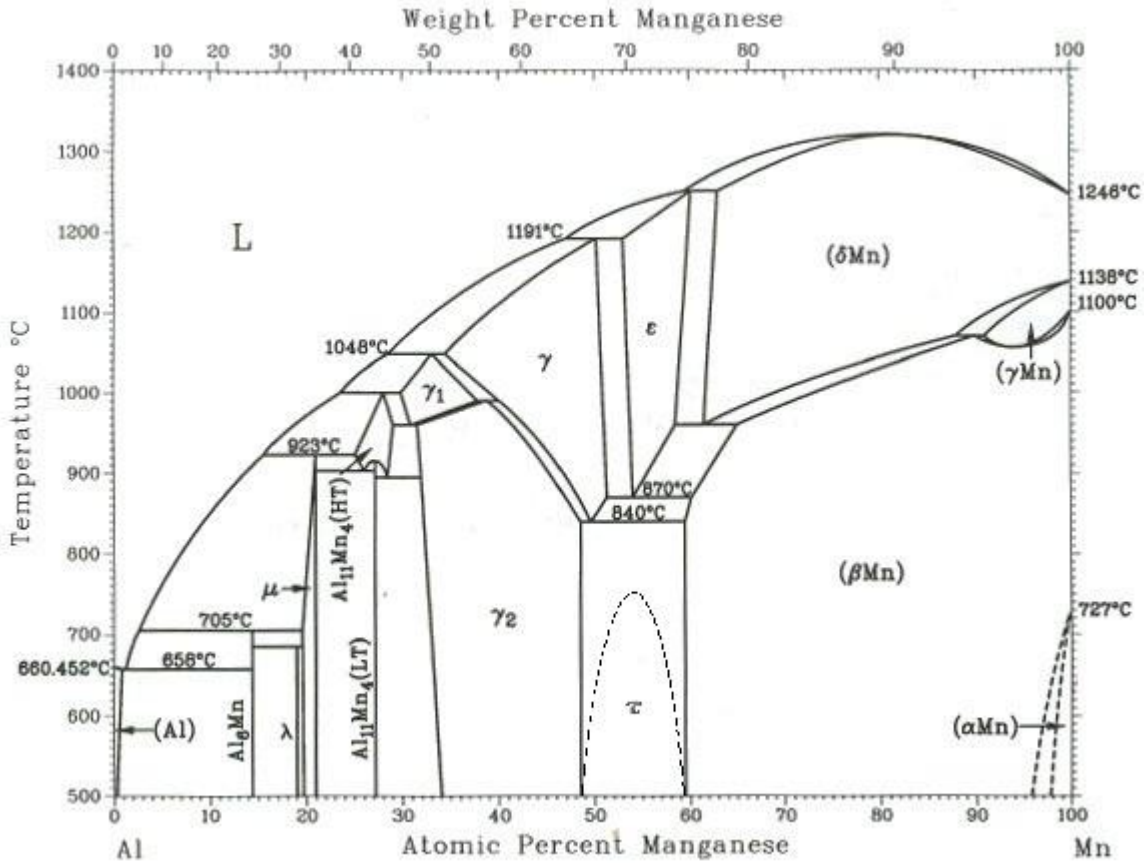

Figure 8 Al-Mn binary phase diagram adapted from [19] with proposed metastable τ-phase region.

Also, as the desired structure is metastable, it has been noted that the addition of small percentages of Carbon will enhance the stability of the τ-phase[13,17,18,20] as well as the saturation magnetization and the moment associated with Mn atoms [13,21]. The latter is substantiated by neutron diffraction data presented by [17] that supports the theory that Carbon atoms occupy the (½,½,½) sites and increase the preference of Mn to occupy the (0,0,0) sites (Figure 9 b). Without these additions the metastable phase will degrade [22] to the equilibrium phases (βMn and $\gamma_2(Al_8Mn_5)$), which can be seen in the phase diagram (Figure 8).

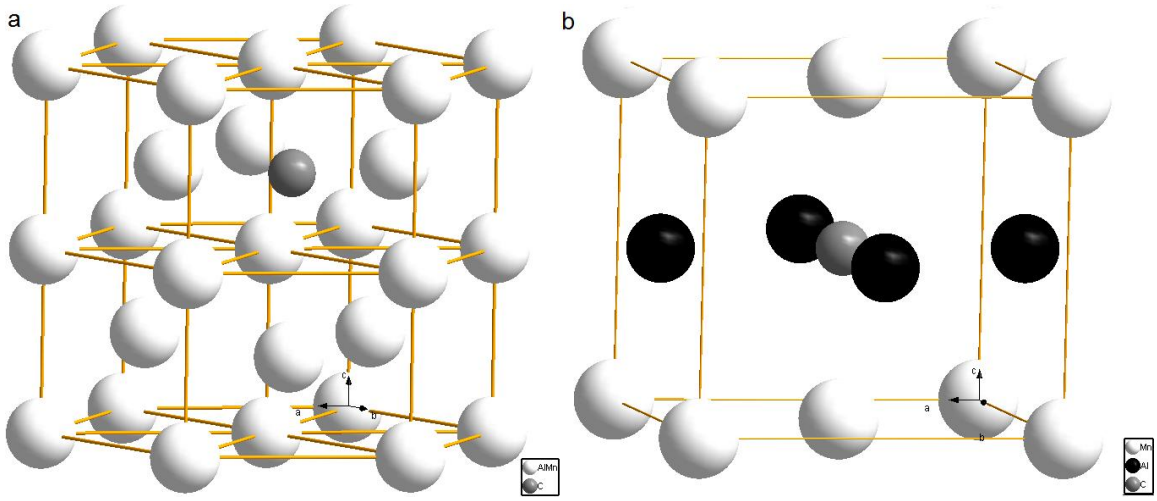

Figure 9 a.) Al/Mn (white) disordered HCP ε-phase with proposed interstitial C (grey). Lattice parameters a and c equal to 2.701 and 4.376 Å respectively. b.) Al (black) and Mn (white) layers in ordered $L1_0$ structure with C (grey) additions in the octahedral interstitial sites. Lattice parameters a and c equal to 3.894 and 3.563 Å respectively.

However, it has been noted also that the addition of Carbon decreases both the Curie temperature (T_c) and the anisotropy field (H_A) [13]. Despite these reductions it is still beneficial to include Carbon for its stabilizing attributes as the formation and retention of the τ-phase is the most important and difficult problem to overcome with the Mn-Al system.

It has been proposed that the τ -phase evolves from the ε-phase in one of two reactions brought on by a heat treatment [22,23]. J.J. van den Broek et. al. [22] in 1979 posited a two-step transition from the hcp ε-phase to the fct τ-phase with an intermediate ordered hcp ε'-phase (Figure 10).

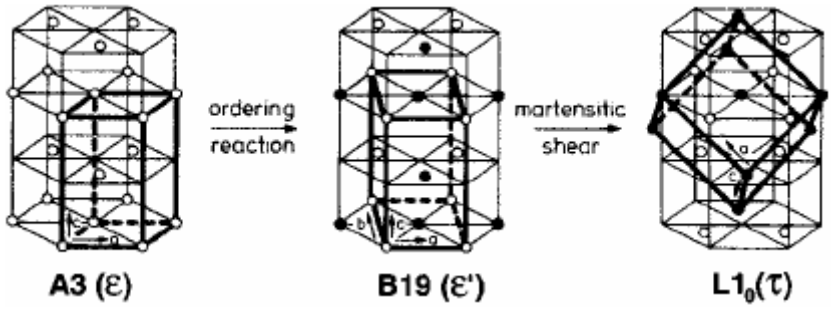

Figure 10 Phase transformation proposed by Broek et. al. [22] with intermediate ordered orthorhombic phase (B19) denoted by ε'.

Transmission electron microscopy (TEM) images have shown the formation of the ε-phase as well as the ε'-phase initially but the conclusion that the transition follows this multi-stage kinetics is undocumented. Dreizler et. al. [20] also subscribes to this method of phase transformation for $Mn_{1-x-y}Al_xC_y$ in the range $0.42 \leq x \leq 0.47$ and $0 \leq y \leq 0.021$ stating that the addition of carbon increases the stability. Also noted was the need for continuity between phase transformation mechanisms at high temperature and low temperature regardless of inherent differences in driving forces. This evolution has also been promulgated by many others in the academic community [8,10,13,15,16,24].

However, in 2002 Yanar et. al. [23] suggested instead that the transformation follows a "massive", compositionally invariant diffusion and growth process that migrates by incoherent interphase interfaces.

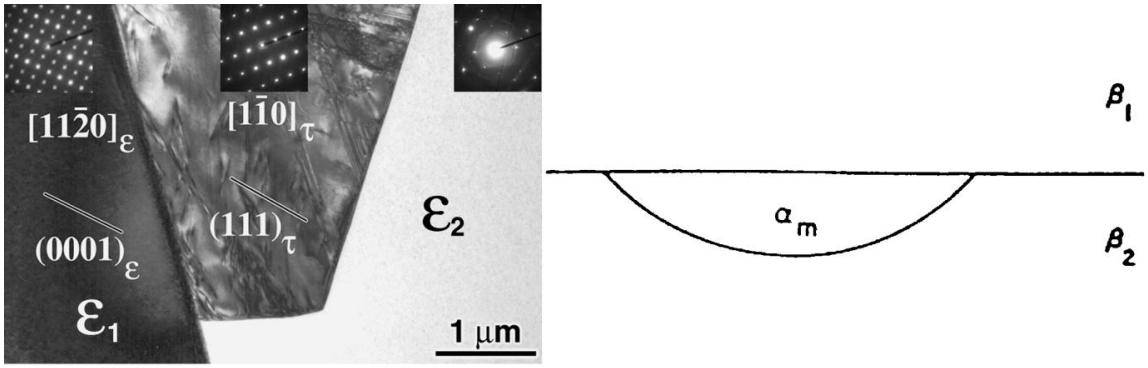

Figure 11 "Massive", compositionally invariant nucleation and growth process proposed by Yanar et. al. [adapted from [23]] with TEM image (left) to substantiate hypothesis (right).

The TEM images presented fully substantiate this hypothesis and suggest a growth that nucleates from grain boundaries and shares some coherency with one grain, but no coherency with the grain that is being consumed. It is assumed that this diffusion-based process begins with a critical nucleus and from classical nucleation theory, the free energy of activation of such a nucleus (ΔG*) follows

$$\Delta G^* = \frac{16\pi\gamma_{\alpha\beta}^3}{3(\Delta G_v + \omega)^2} \cdot K, \quad (6)$$

where $\gamma_{\alpha\beta}$ is the interfacial free energy (between α and β phases in Figure 11 b), ΔG_v is the volume free energy released, ω is the volume strain energy, and K is a geometry factor based upon the ratio of the volume of the critical nucleus to the volume of a spherical nucleus. Shown in Figure 11 is a singly-faceted nucleus which is predicted when the free energy between the coherent grains ($\gamma_{\alpha\beta}^c$) is less than or equal to half that of the initial grains ($\gamma_{\beta\beta}$) or,

$$\gamma_{\alpha\beta}^c \leq 0.5\gamma_{\beta\beta}. \quad (7)$$

Finally, the activation enthalpy for boundary diffusion (ΔH_D) was calculated using a modified Burke-Turnbull equation as 154 KJ/mol, which was considered to be reasonable for boundary diffusion.

The τ-phase has been shown to evolve through two different annealing methods; short time annealing (around 500°C) which provides just enough energy for the $L1_o$ structure to grow, or slow cooling from high temperature (>700°C) [8]. Either of these methods will result in the ordered face-centered tetragonal (fct) $L1_o$ τ-phase which exhibits ferromagnetism. If the alloy is allowed to slow cool from high temperature, the grains will grow in size and become much larger than the other case. Therefore, the method that will be outlined here is following the first process (short term, low temperature annealing after formation of the parent ε-phase) due to the grain size dependence on the magnetic properties (namely the coercivity). There are few methods in which to increase the magnetic properties of a specific alloy/structure including mechanical milling (pre- or post-heat treatment), hot extruding, and various methods of deposition (i.e. vapor, electrolytic). However, post processing in the field of nano-structured bulk magnets consists traditionally of mechanical milling which reduces the grain size to that of a single magnetic domain which can improve the magnetic properties [1]. However, historically and theoretically there exists a lower limit to the optimum size of the powder below which the material becomes superparamagnetic (SP) [1] and therefore unfit for permanent magnet applications.

Chapter 2

EXPERIMENTAL

2.1Materials

Mn, Al, B, and C were procured from Alfa Aesar at 99.9%, 99.999%, 99.5%, and 99.9995% purity respectively; however, the manganese was cleaned with Nital (1% vol. Nitric Acid) in an ultrasonic cleaner due to oxidation occurring in air. Heptane (99.9%) and Oleic acid (99.9%) for surfactant assisted ball milling were procured from Fischer Scientific.

2.2Processing

2.2.1 Arc Melting

Arc Melting is a process whereby high precision alloys can be formed with a large degree of homogeneity. Elements that are weighed out in a certain composition are placed onto a water-cooled copper base (grounded) and the whole thing is placed under vacuum. A water-cooled electrode that can be manipulated from outside the vacuum chamber is equipped with a tungsten tip and held in place with a copper sleeve and fastener. Tungsten, with a melting temperature of 3422 °C is a perfect material for conducting the current as it will melt at higher temperatures than most alloys and much higher than the alloy in this report. The chamber is evacuated and backfilled to ensure all oxygen content is reduced to a minimum level. A figurative depiction of the arc melting setup used in this

report can be seen in Figure 12 alongside a picture of the actual setup during melting. The purpose and goal of arc melting is to create an alloy as homogeneous as possible; therefore, while melting the material, a circular motion is used to physically mix the melt with the plasma. Once this is done, the alloy is allowed to cool in the chamber for a long time (ab. 5 min.) so that when it is exposed to air it does not oxidize. Arc melting was carried out in a homemade apparatus, with a Miller Syncrowave 180SD power supply which is capable of 150 Amps at 26 Volts. It is useful to note at this point that real changes in composition can occur during the arc melting process due to vaporization of some metals (e.g. manganese). This can be compensated by addition of extra material, and has been done in this case in the amount of 3wt% Mn. This number is derived from weighing the constituent elements before and after melting for multiple samples.

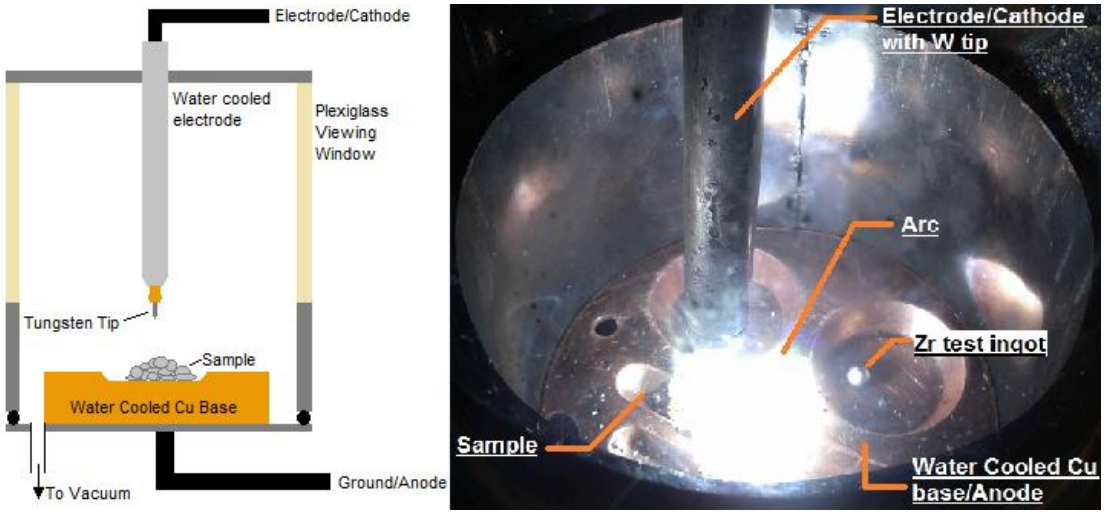

Figure 12 Arc Melting diagram on left, and picture of actual melting on right.

2.2.2 Melt Spinning

Melt spinning is a rapid solidification process in which molten metal is shot out of a small hole in a quartz crucible onto a spinning wheel of copper. The resultant metal is cooled at rates upwards of $1x10^6$ °C/s which, for some alloys creates an amorphous material and for others greatly reduces the grain size. In this study, it is used for the latter purpose as a small grain size increases the magnetic properties [1]. Also, the extreme undercooling can bypass phase formation to retain metastable phases, as is necessary for this system. Furthermore, the formation of small grains of the metastable ε-phase directly correlates to small grains of τ-phase even after grain growth during the annealing process. The metal is melted with a high voltage, high amperage source induction melting coil which induces a current in the metal which drives up the temperature due to electrical resistance in the metal itself. Once the metal is molten, a pressure container (Δ0.2 bar of Argon) is connected to the crucible and the pressure differential between the inside of the crucible and the rest of the chamber forces the melt out of the orifice at high rates. The copper wheel rotates at a velocity (measured from the surface) anywhere between 0 and 40m/s and this parameter directly effects the cooling rate of the machine. Melt Spinning was done by an S1 Edmund-Buhler Gmbh melt spinner (Figure 13 a) in an inert Argon atmosphere at 40m/s (unless otherwise specified), a diagram of the melt spinning apparatus can be found in Figure 13 b with all of the main components necessary for the melt spinning process. The resultant ribbons (Figure 13 c) that are formed can be characterized as is or powdered and then characterized (this is referred to as the as spun (AS) state hereafter).

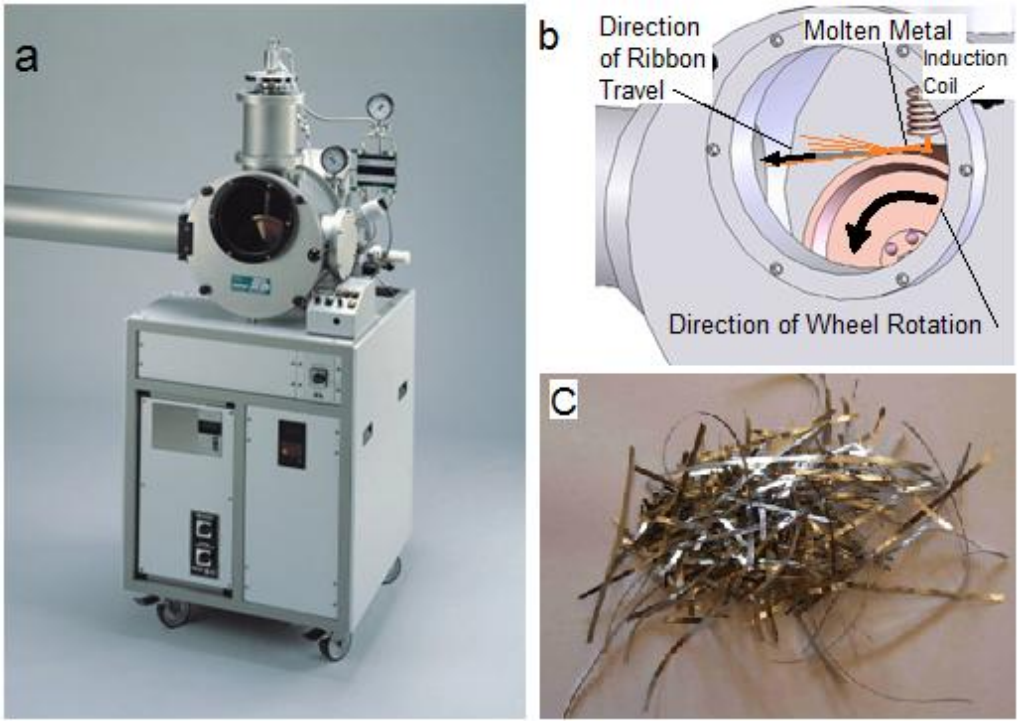

Figure 13 a.) Melt Spinner by Edmund Bühler GmbH b.) Diagram of Melt spinning procedure molten metal is forced out of a quartz crucible onto rotating wheel, cooled and directed down tube to left c.) melt spun ribbons

It should be noted that many variables exist in the melt spinning process, and some deviations from the idea case are present. For example, the sample can easily be overheated in which case the wheel does not sufficiently undercool the sample which is necessary for formation of the ε-phase. As will be discussed later, many batches must be made to ensure the reproducibility of the experiment.

2.2.3 Mechanical Milling

Mechanical milling, or high energy ball milling (HEBM) is a processing technique in which ball bearings are placed in a vial along with a sample (in this case ground ribbons from melt spinning)

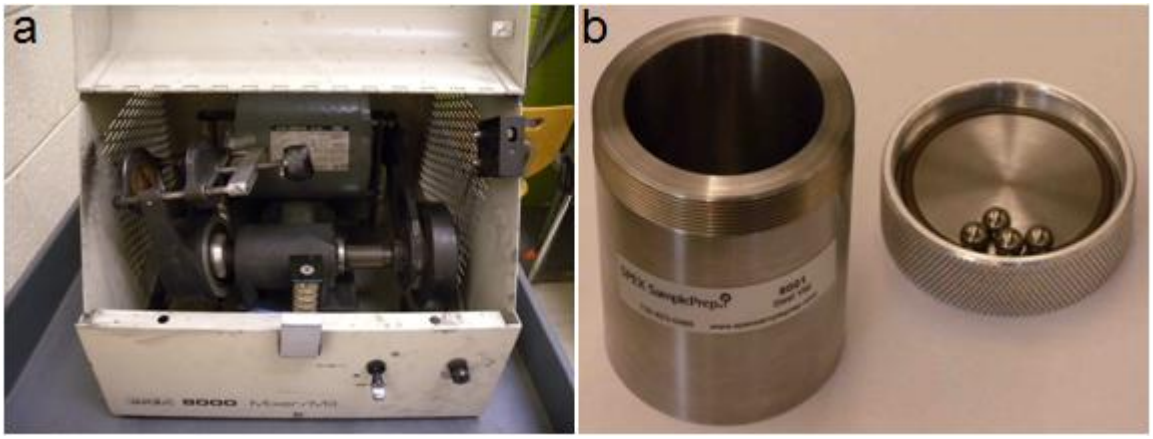

Figure 14 a.) SPEX SamplePrep Mixer/Mill 8000 and b.) Steel Vial with 4mm dia. ball bearings

Ball milling was carried out in a SPEX 8000 mechanical mill (Figure 14 a) and milling vials (Figure 14 b) were sealed under an inert gas (Argon or Nitrogen) atmosphere. The mills were controlled by a PC to run 10 minutes at a time with 5 minutes cool down time between cycles. The vials used for milling are made of hardened steel and the ball bearings are 4mm in diameter and each weight 1.1g. The size of balls was chosen to maintain a 10:1 mass ratio between the balls and the powder due to the small sample size being milled at one time.

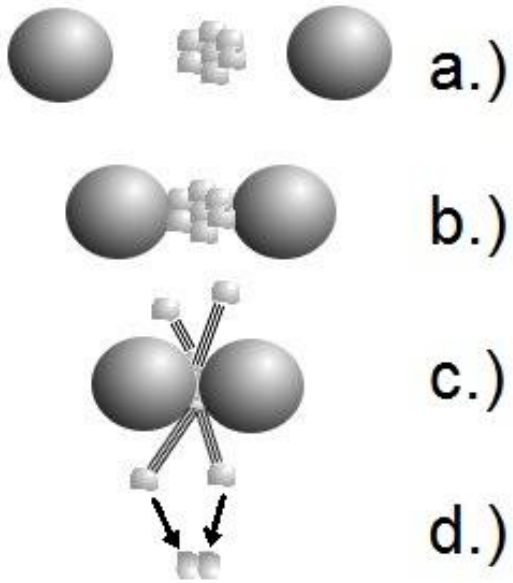

Figure 15 a.) Components of mechanical milling before impact b.) elastic compression of particle c.) plastic deformation and breaking of particle into smaller pieces (individual grains) d.) rewelding of individual grains

2.2.3.1 Nonreactive Gas

Mechanical milling involves a high energy setup where a hardened steel vial is shook at high rates causing the ball bearings within to impact the inner walls of the vial at high velocities. This impact physically grinds the contained powder down to nanometer-scale particles; however there is a limit to the ability of the mill to reduce particle size at which individual particles reweld (Figure 15) to form larger multiple grain/domain particles. During this process large amounts of heat are produced from the impacts and both oxidation and vaporization of the material can occur. To alleviate this, the vial is sealed in a nonreactive gas atmosphere and the milling is done in increments with a cooling period after 10 minutes of continuous milling.

2.2.3.2 Surfactant Assisted

As mentioned previously, there is a limit to the particle size that can be created by mechanical milling. To get around this limit surfactants are used to keep the particles from reforming. In this report Oleic acid (OA) was used as a surfactant (5wt.% of the powder) and heptane was used as a milling medium. The same procedure for milling as used without surfactant was used with surfactant (10 min on 5 min cooling). Upon completion of milling the resultant slurry was washed several times with heptanes then acetone to remove the oleic acid and subsequently dried.

2.3Characterization

2.3.1 XRD

As x-rays are incident upon a crystalline lattice something special happens, interference between x-rays reflected off atoms in crystalline planes occurs. This interference follows Bragg's Law, where two incident beams either cancel each other out, or augment each other creating a peak at specific values of 2θ for a given crystal lattice when plotting Intensity vs. 2θ. The relation being

$$2d \sin\theta = n\lambda \quad (8)$$

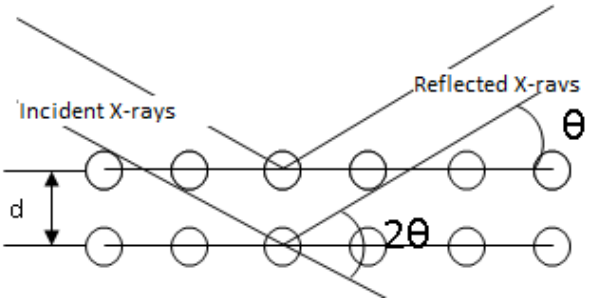

Figure 16 Bragg diffraction due to atoms in a crystalline lattice.

where, d is the interplanar spacing, θ is the angle of incidence, λ the wavelength of x-ray, and n is an integer (1, 2, 3 …). It is the peaks in an XRD pattern that make it possible to identify alloys and crystalline structures present in a material. For powder samples (as are discussed in this report) the peaks are broadened (due to random crystal orientation and strain), and with some assumptions, the average size of the particles and the strain in the crystals as well as the lattice parameter can be calculated. XRD patterns were captured with a Rigaku Multiflex diffractometer with a copper target operating at 1.54242 and 1.566310Å for $CuK\alpha_1$ and $CuK\alpha_2$ respectively.

2.3.1.1 Diffraction Pattern Analysis

To obtain useful data from a pattern one must first take into account the impact of the x-ray diffractometer itself. A sample of LaB_6 is scanned with the instrument and, since LaB_6 is free of microstrain, the resulting differences in peak position (2θ) and full width at half max (FWHM) are due to the machine alone. Peaks observed in XRD patterns include contributions from two types of peaks, Gaussian, and Lorentzian and each has a different characteristic peak width ($H_G(\theta)$ and $H_L(\theta)$, respectively). These two contributions are convolved together and must be separated. In this case the width correction for the instrument is:

$$H_G^2(\theta) = (0.03003 \tan\theta - 0.04259)\tan\theta + 0.02644 \qquad (9)$$

and, $H_L(\theta) = 0$, which are calculated from the LaB_6 pattern. However, to strip the strain effects on the peak broadening the Scherrer formula must be abandoned in favor of a Williamson-Hall method modified by Langford

Using FullProf Sute's WinPLOTR software, the instrumental peak broadening effects can be stripped, and the corrected FWHM ($\beta_{corrected}$) can be recorded for each peak in a specific diffraction pattern. If this method is not available, then the βcorrected can be calculated from a convolution of the experimentally measured FWHM (β_{ex}) and the instrumental peak broadening (β_{instr}) by the following,

$$\beta_{corrected} = \beta_{ex} - \frac{{\beta_{instr}}^2}{\beta_{ex}}. \quad (10)$$

Then using the Williamson-Hall method modified by J.I. Langford[25] the following is plotted $\left[\left(\frac{\beta^*}{d^*}\right)^2 = f\left(\frac{\beta^*}{(d^*)^2}\right)\right]$ such that,

$$\left(\frac{\beta^*}{d^*}\right)^2 = \left(\frac{1}{\varepsilon}\right)\frac{\beta^*}{(d^*)^2} + \left(\frac{\eta}{2}\right)^2 \quad (11)$$

where,
$$\beta^* = \frac{\beta_{corrected}\cos\theta}{\lambda} \quad (12)$$

and,
$$d^* = \frac{2\sin\theta}{\lambda} \quad (13)$$

The stress η can be determined from the intersection of the trace with the y-axis, and the slope (1/ε) is related to the size of the crystallites. For spherical particles/grains the relations is as follows:

$$r = \frac{4\varepsilon}{3} \quad (14)$$

where r is the diameter of a spherical particle, and ε is the inverse of the slope of the above trace.

2.3.2 Differential thermal analysis (DTA)

DTA consists of a furnace, two thermocouples and a chamber that can be filled with a specific gas (Argon in this study). Aluminum oxide crucibles are used as sample holders, one filled with aluminum oxide powder, and the other with a small amount (~50mg) of sample and covered with aluminum oxide powder. The two crucibles are placed in contact with the thermocouples and the chamber is closed and covered with the furnace. The data recovered is the temperature difference between the two thermocouples which can be converted to the heat flow to and from the sample through a heating regime. In this study the heating rate is 10°C/min and the range was from 300-900°C and all tests were carried out on a DTA7 from PerkinElmer under Argon atmosphere at a flow rate of 20ml/min.

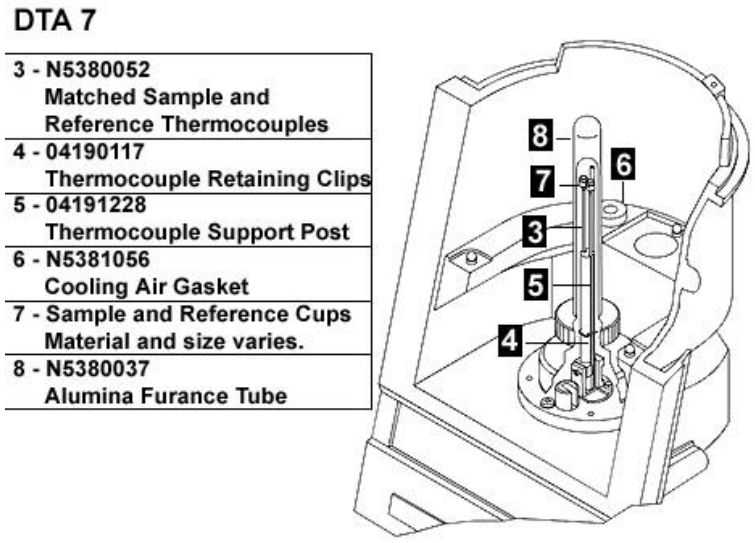

Figure 17 DTA 7 internal setup showing sample and reference placement inside furnace tube (controlled atmosphere).

2.3.3 Thermo gravimetric Analysis (TGA)

Thermo gravimetric analysis determines degradation properties based upon an accelerated degradation process measuring the change in mass over a large temperature range (usually RT 25°C to 700°C). The mass that remains after the test is (depending on the atmosphere in which the test is done) the part that will not degrade easily. The time-temperature similarity can be used to estimate the amount of time it would take for the sample to degrade at RT in a given atmosphere. The machine used for this report was a STA6000 produced by PerkinElmer.

2.3.4 Microscopy

2.3.4.1 Light Microscopy

The principles of light microscopy are well known and widely used for a variety of application and thus will not be explained in this report. The samples were observed with a Leica DM2500M and captured with a Leica DFC290 camera. Images were taken of surfaces etched with Poulton's reagent as prescribed for aluminum alloys by [26].The images were taken under polarized light unless otherwise specified.

2.3.4.2 Scanning Electron Microscopy

A scanning electron microscope (SEM) is a versatile tool that can be capable of resolving images from 50x to 300000x and beyond. The electron beam is concentrated and focused on the target by electromagnetic lenses. The electrons then interact with the target (Auger electrons, back scattered electrons, and secondary electrons) and the electrons leaving the surface are collected by a sensor. The intensity of electrons caught by the sensor is directly related to the intensity of the corresponding spot on the screen. The scan rate of

the electron beam on the surface of the sample is synchronized with the positioning on a computer screen to create an image. The instrument used for the purposes of this report was an FEI NanoSEM equipped with an Energy-dispersive X-ray Spectrometer (EDX or EDS). EDS works by collecting x-rays that are emitted from a material when bombarded with an energy source (in this case an electron beam). When an electron from the incident beam knocks an electron from the orbital of an atom the electrons in the higher bands fill the gap. When an electron lowers its energy by dropping to a lower energy state it emits a photon in the form of a very specific wavelength (x-ray) that can be measured. From this information a pattern can be created with peaks at certain energy levels and the relative intensity of the peaks can be correlated to the relative content of each element in the material.

2.3.5 Magnetic Measurements

The extrinsic magnetic moment of a material can be measured to determine its intrinsic properties (e.g. Anisotropy Energy (K), Saturation Magnetization (M_s), Curie Temperature (T_c)). This is done by applying an external magnetic field and measuring the magnetization of the material itself. There are a number of ways to achieve this from the most accurate (SQUID) to the quickest but not so accurate (AGFM). However, it is necessary to pulse magnetize certain samples that have a saturating field higher than the maximum field a magnetometer can apply. Pulse magnetization is a procedure by which a sample is exposed to a very high magnetic field for a short amount of time. This is done with a large bank of capacitors that accumulate charge and a large electromagnet that must be water cooled due to the high current required to generate the field. The pulse

magnetizer used in this study is capable of applying a field of 125kOe which is more than enough to saturate Mn-Al [5]. The samples created for magnetic measurements in this study were all weighed in a microbalance (accuracy ±1 μg) aligned in a magnetic field and sealed in adhesive (super glue). The procedure for this sample preparation can be seen in Figure 18.

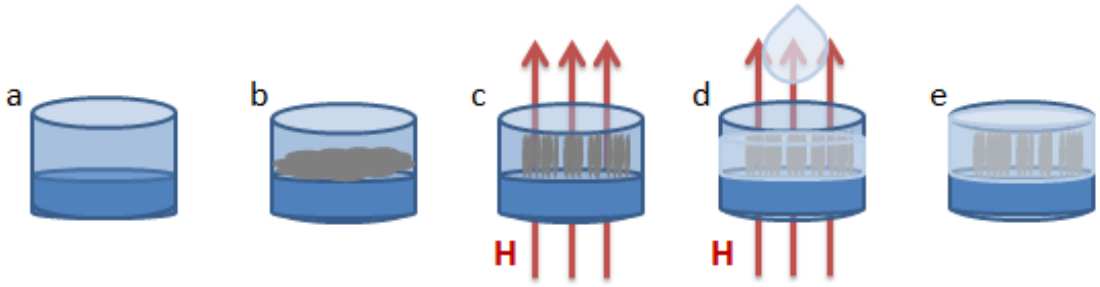

Figure 18 Magnetic characterization sample preparation. a.) sample cup is made and balance is tared to its weight b.) sample is placed into cup and sample mass is weighed c.) magnetic field is applied and sample aligned d.) adhesive is applied while particles are still aligned e.) finished sample with aligned particles sealed in adhesive.

2.3.5.1 AGFM

An Alternating Gradient Field Magnetometer (AGFM) was used primarily to determine the coercivity of the various samples. As the name implies it uses an alternating magnetic field to vibrate the sample back and forth while under an external DC magnetic field (0 to 11kOe (1.1T)). The sample probe is attached to a piezoelectric sensor so that the vibration of the sample can be translated into an electric current which data acquisition software can then decipher into a magnetization value for the sample. The coercivity of the sample can be determined within acceptable limits, however the saturation magnetization value cannot be trusted, therefore for this study all AGFM hysteresis loops

will be normalized. Because the reading of the magnetic moment of the material is calculated from electrical signals from the piezoelectric sensor there is some inherent error in the system and the machine must be calibrated with a well defined sample of nickel. Also, the loop is usually adjusted to subtract paramagnetic or diamagnetic slope changes that are present due to sample preparation (e.g. glass, plastic or epoxy).

2.3.5.2 SQUID

The Superconducting QUantum Interference Device (SQUID) is a device used to measure the magnetic properties of a small sample. A sample is lowered into a Dewar capable of temperatures from 4K to 400K (-269°C to 127°C). Once between the superconducting coils, the sample is subjected to an external magnetic field. This applied field elicits a response from the material and this response is measured by the previously mentioned superconducting coils. The applied field and the temperature of the sample can be manipulated independently resulting in a number of tests that can be preformed. However, for the purpose of this study only hysteresis loops at RT (300K) were recorded; meaning the magnetic field was varied from 7 T to -7 T and back to create a full hysteresis loop. The unit used to test samples for this report was a Quantum Design MPMS with an applied field range of ±7 T and a temperature range of 4K to 400K. The device has a DC Magnetization absolute sensitivity of 1×10^{-8} emu at 25,000 Oe (equal to 2.5 T) which is well below the values that will be reported here and two sample transports (either a Reciprocating Sample Option (RSO) or a standard (DC) transport head). Knowing both τ and (100s and τ_0 is 10^{-9}s, respectively, for SQUID measurements)

and considering only uniaxial particles the Neel-Brown relation (4) can be solved for the blocking temperature [1],

$$T_B = \frac{KV}{25k}. \tag{15}$$

Chapter 3

RESULTS

First of all it is necessary to understand the transition from the ε to τ-phase the implications this transition has for experimental measurements. Many of the XRD patterns shown here will be selections of the high intensity peak region. In this region between 38 and 50° 2θ, the highest intensity peaks for all the phases that are interesting to the study can be found (ε, τ, γ2, β). A typical XRD pattern for ~95% phase pure samples can be found in Figure 19. What should be noted is the formation of the equilibrium βMn phase in the upper pattern at about 42.5 and 45 ° 2θ; at less than 5% the height of the highest τ-phase grain this sample is almost "phase-pure."

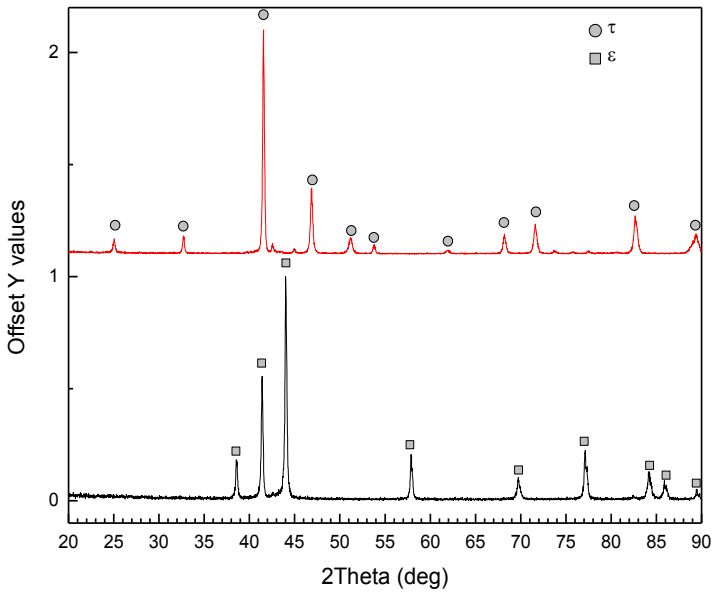

Figure 19 Typical transition from the ε-phase to the τ-phase.

3.1Addition of Boron vs. Carbon

It has long been known that additions of certain elements to alloys can increase desired properties like hardness or workability, corrosion resistance; unfortunately it is difficult to determine which element will aid and which will not. Therefore, metallurgists tend to follow a trial and error method; however, modern metallurgy demands alloys be created to perform specific tasks, and to do this they must be formulated with a scientific process. The addition of carbon to the Mn-Al system has been shown to stabilize the otherwise metastable ε-phase (and therefore the τ-phase as well) [8], as well as increase the saturation magnetization; however, it reduces both the Curie temperature and the anisotropy field [16]. The thought is that elements of similar atomic number and radius should have a similar effect on the alloy; therefore, in this study, the substitution of boron for carbon to the alloy was attempted. First analysis of this alloy demanded a rough set of mixtures (three data points over a large composition range). As has been reported before, manganese and aluminum in the near equiatomic region has yielded the FM τ-phase. From the starting point of $Mn_{54}Al_{46-x}C_x$ with x=2 carbon was substituted by boron yielding three distinct nominal alloys: $Mn_{54}Al_{44}C_2$, $Mn_{54}Al_{44}B_1C_1$, and $Mn_{54}Al_{44}B_2$. Each batch was characterized with the XRD in its as spun (AS) state to determine the phase purity and amount of ε-phase present. The three alloys were then characterized using DTA to determine the temperature of the phase transformation $\varepsilon \rightarrow \tau$, if possible, and annealed to attain the τ-phase. The XRD pattern of each sample was then collected to be sure of the present phases and the alloys magnetic properties were measured before and after the annealing process.

3.1.1 Melt Spinning Results

Manganese aluminum carbon and boron were first arc melted in their respective compositions and then melt spun into ribbons. At this point XRD was performed to determine if the ε-phase was attained as this has been well documented in literature. Also, multiple batches were prepared to give statistical importance to the results.

In the case of MnAlC, as has been seen in the literature, the addition of carbon stabilizes the parent ε-phase and helps stabilize the formation and retention of the τ-phase. For the melt spun samples with only carbon additions all four batches contained ε-phase and only batch 2 showed signs of the equilibrium γ_2-phase (Figure 20). The discrepancies in peak position and phase purity with each subsequent batch are evidence of the difficulty of sample preparation. Even though every sample was prepared with the same procedure, each one exhibits slightly different peak positions due to measurement error or by real changes in the composition during fabrication (Mn loss). These discrepancies are more evident in the samples containing boron.

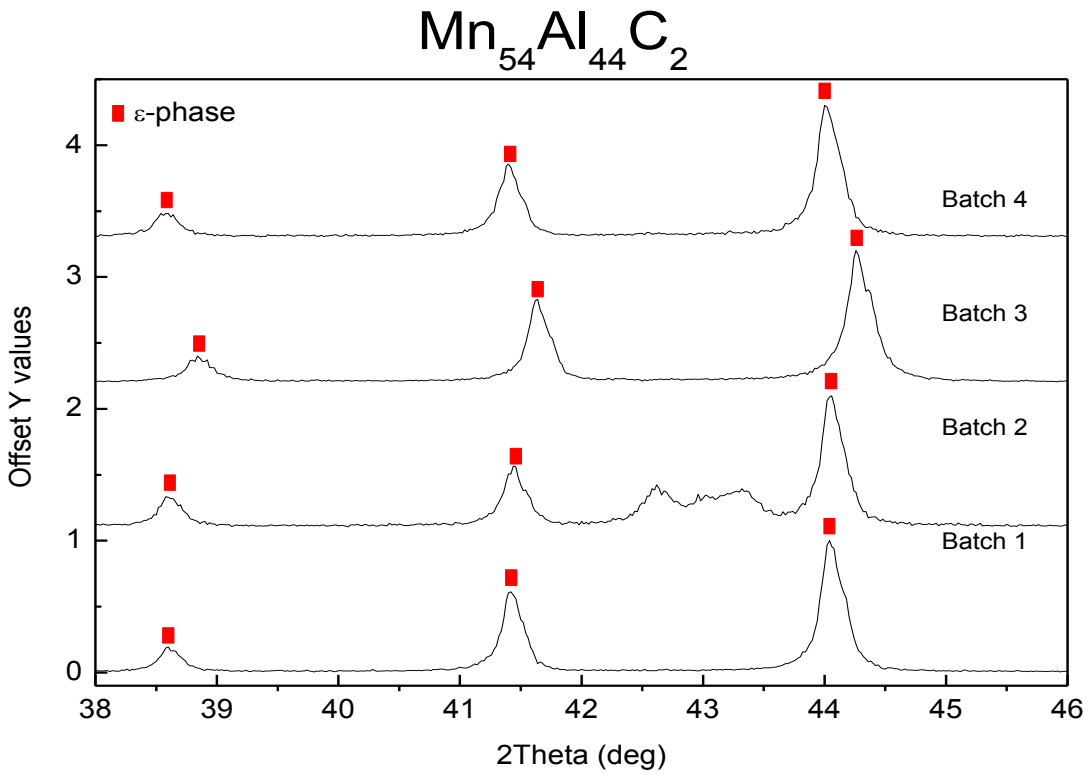

Figure 20 XRD patterns for selected samples of C-doped AS samples with minimal impurities or peak shifts.

In the case of MnAlBC there is still a peak shift between the batches, and one sample contains a large amount of equilibrium phase (γ_2) (Figure 21). However, all samples contained ε-phase and only one batch contained a majority of equilibrium phase. Due to this it is apparent that even small amounts (less than the solubility limit of carbon in Mn-Al) of carbon can still stabilize the ε-phase; however, the influence on the magnetic properties will be reported later in this section.

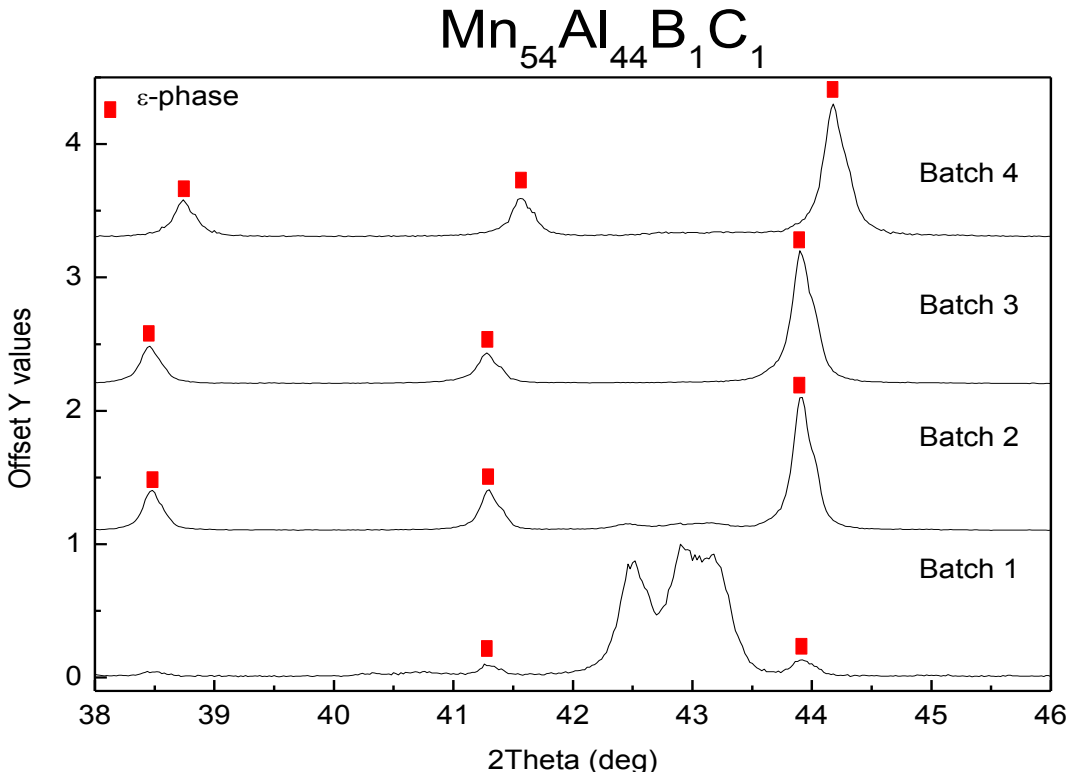

Figure 21 XRD patterns for selected B and C doped AS samples from multiple batches. Notice phase purity in all but one batch.

Five batches of MnAlB can be seen in Figure 22, wherein only three exhibit the ε-phase and only one of which contains less than 20% other phases. There is also an apparent shift in the peak position of the ε-phase peaks as well as the equilibrium phases and no clear influence of boron on the formation of the room temperature ε-phase. Therefore, more work must be done to characterize the phase transformations in all three systems explored here.

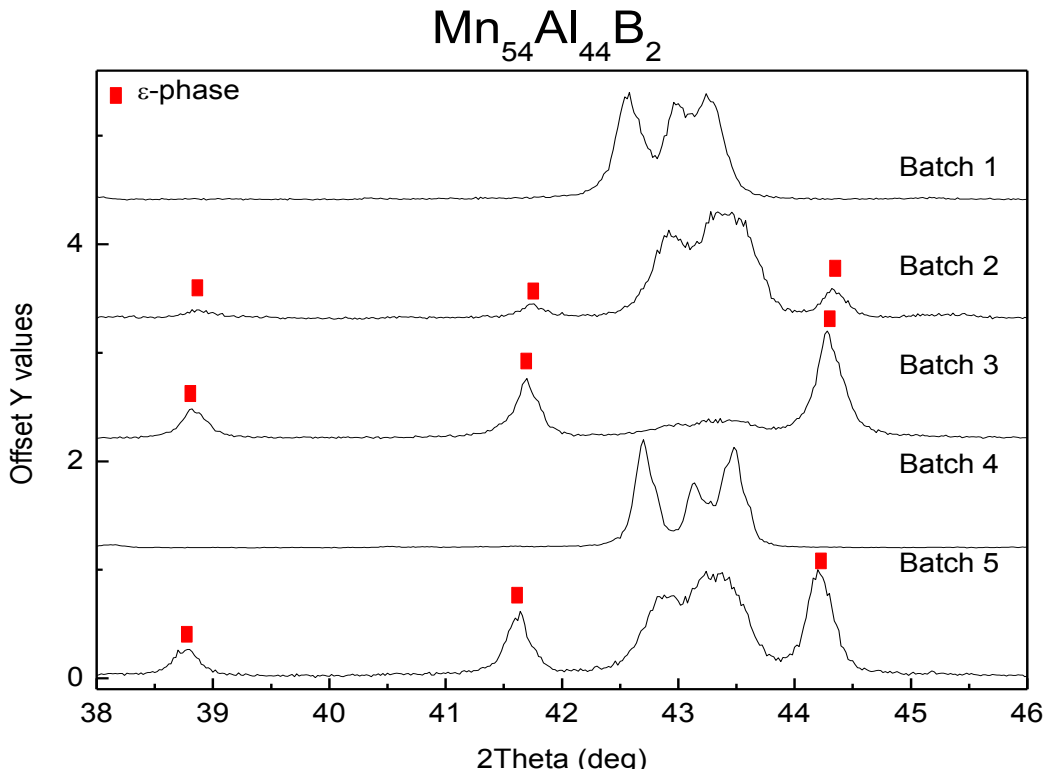

Figure 22 Selection of XRD patterns for B-doped AS samples. Notice different phase composition for each batch.

It is evident that discrepancies between batches should be avoided at all costs; however, it is inevitable for there to be error in experimental science. The peak shifts are due to slight changes in composition during arc-melting where Mn can easily vaporize. To alleviate this problem excess Mn (~3 wt%) is added to the material before melting, which should make up for any lost material. The formation of the equilibrium phases can be due to compositional fluctuations or due to poor melt-spinning techniques. If the melt is not completely transformed into ribbons then the material is not cooled at the maximum rate which gives the material enough time to form the equilibrium phases that would normally form

3.1.2 Phase Transformation Kinetics

DTA has been used previously to determine the phase transformation kinetics of the Mn-Al system; therefore it was interesting to see the DTA curves for the different alloys containing boron and carbon. Once the successful formation of the ε-phase was complete, DTA analysis was conducted to determine the phase transformation characteristics (e.g. stability) from which optimal heat treatment parameters can be derived. As can be seen in Figure 23, the addition of carbon completely changes the transformation kinetics from multiple peaks, to a simpler curve with a reversible two peak system; ε→τ (at around 500C) and τ→ε (at around 800C). However, in all cases the eutectoid reactions are apparent in the 800-900°C region where the metastable phases (ε or τ) decompose into a combination of either γ + β or γ_2 + β. In the case of $Mn_{54}Al_{44}B_2$ it can be seen from the phase diagram for Mn-Al that the τ-phase exists in the two-phase region between the γ_2 and βMn phases. However, the XRD pattern of a sample of $Mn_{54}Al_{44}B_2$ annealed for 1 hour at 750°C exhibits only βMn-phase peaks. This discrepancy could be due to a β-phase preferential composition change (i.e. to the right in Figure 25) or a fundamental change in phase diagram due to the addition of boron (Figure 25 b).

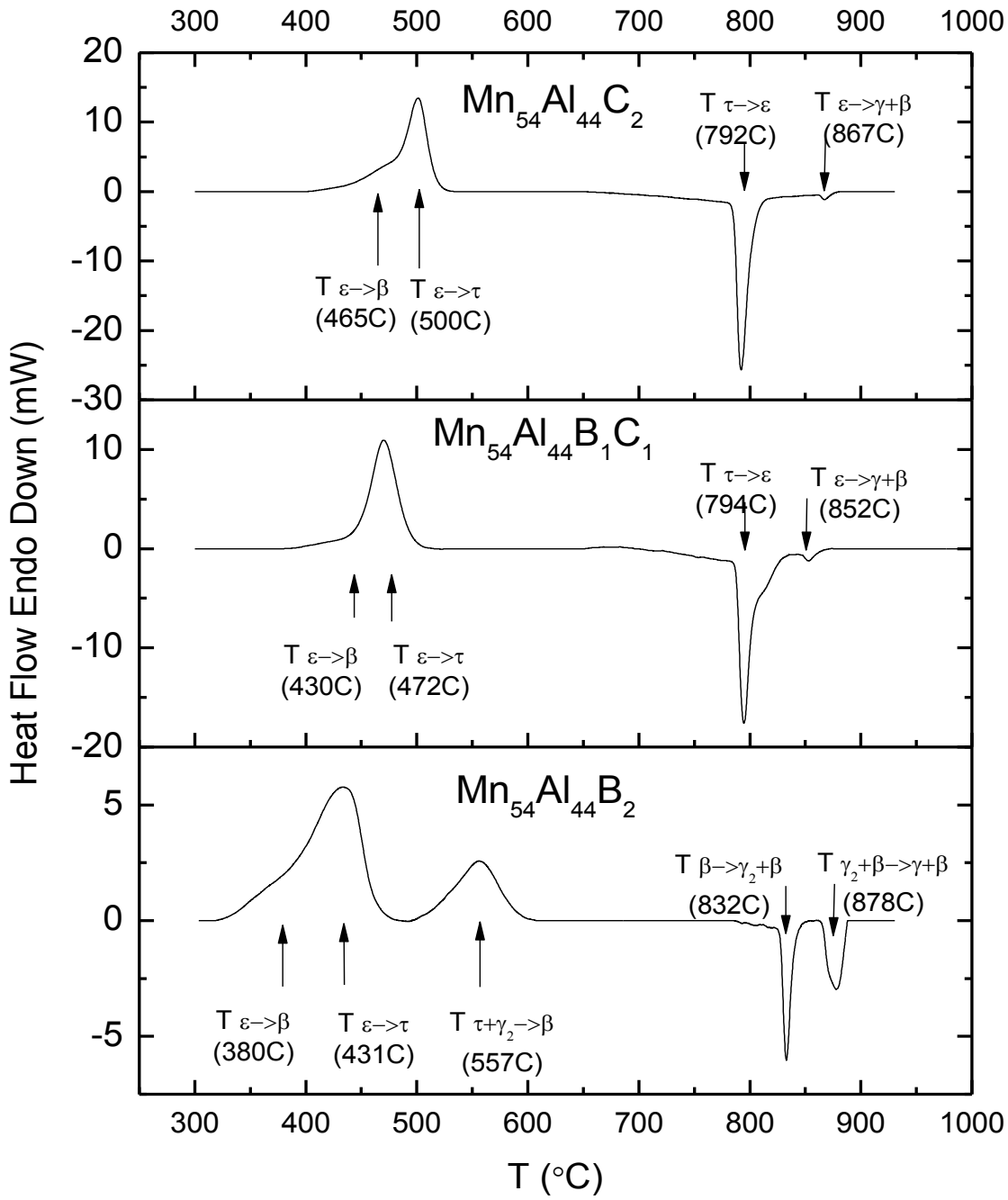

Figure 23 DTA curves for each sample composition, note the complexity of the MnAlB system when compared to the carbon doped systems. Also, MnAlB exhibits full decomposition of τ-phase at 557°C.

3.1.3 Heat Treatment

Once the DTA curves for each composition were determined, the optimum annealing temperature could be prescribed for each sample. However, each AS sample was annealed at 500C for 10 minutes which, based upon the XRD patterns, was sufficient for the phase transformation to occur (Figure 24). Figure 24 a, the Mn-Al-C alloy in the AS form exhibits phase purity in the ε-phase, and ≈5% (by intensity) β-phase is present in the annealed pattern. This has been attributed to the stabilization effects of carbon on the formation of the metastable phases and is also apparent for the Mn-Al-B-C alloy in the middle of Figure 24. Although there is more β-phase the addition of both carbon and boron has a similar effect as to adding only carbon.

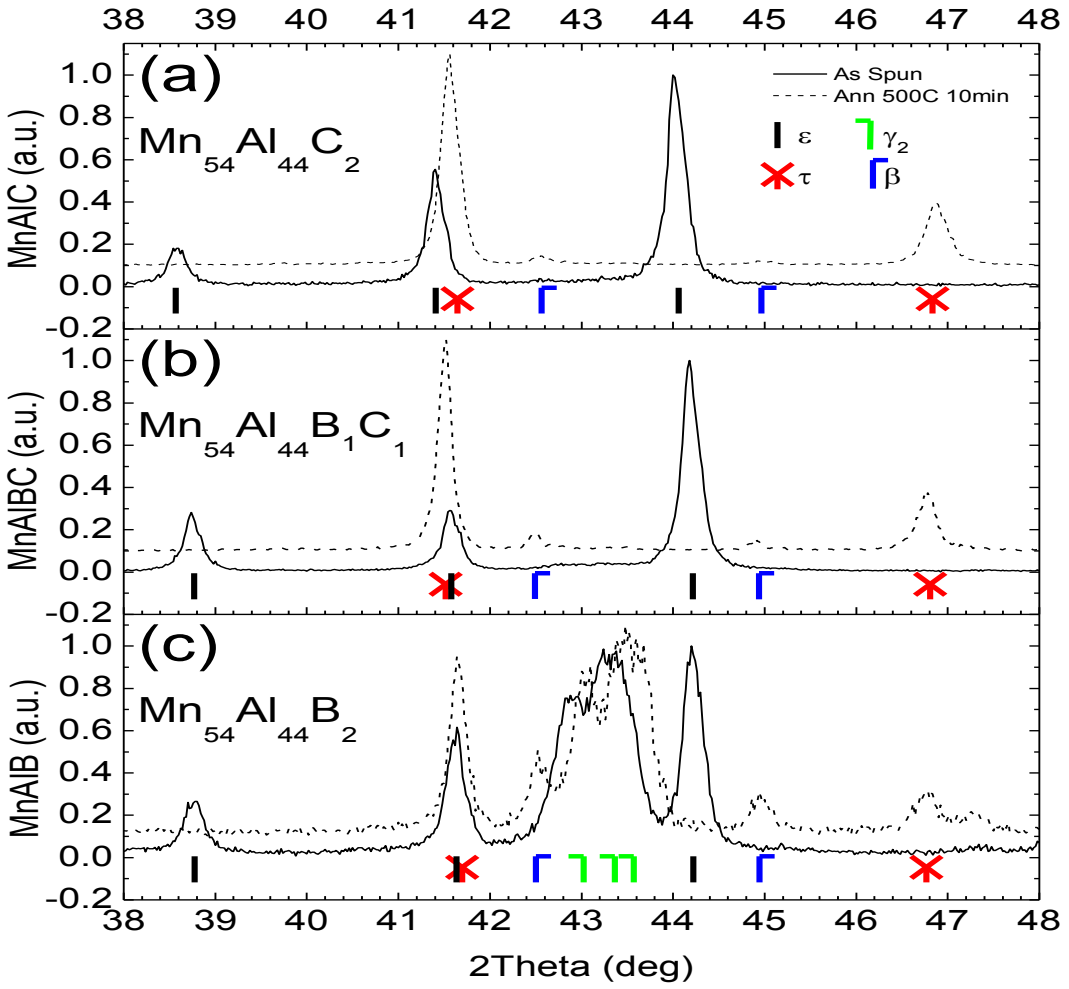

Figure 24 XRD patterns for AS and Annealed (@500C for 10min) samples of each composition: a.) $Mn_{54}Al_{44}C_2$ b.) $Mn_{54}Al_{44}B_1C_1$ c.) $Mn_{54}Al_{44}B_2$. Mn-Al-B shows high percentages of equilibrium phases before and after annealing.

However, when compared to the Mn-Al-B alloy it is apparent that boron has little effect on the stabilization of the metastable phases (τ and ε) that are important. The absence of carbon elicits the formation of γ_2-phase upon cooling (ab. 50/50 between γ_2 and ε) in the AS case and allows the formation of β-phase upon heat treatment (18% β, 38% τ, and

44% γ_2 from peak intensity). Therefore, from the XRD patterns in Figure 24 the only thing that can be said for certain is that the addition of boron does not stabilize the formation of the metastable phases. However, it can be posited with some certainty that the addition of boron does destabilize the ε-phase and therefore, upon cooling, the sample with boron transforms partially into the γ_2-phase; whereas the formation of the β-phase is present upon annealing in all samples. Suggesting that a composition factor is at play here, where the composition being used is closer to the βMn single phase region (Figure 25) or the addition of boron actually changes the phase diagram, and shifts the line between the βMn region and the two-phase region.

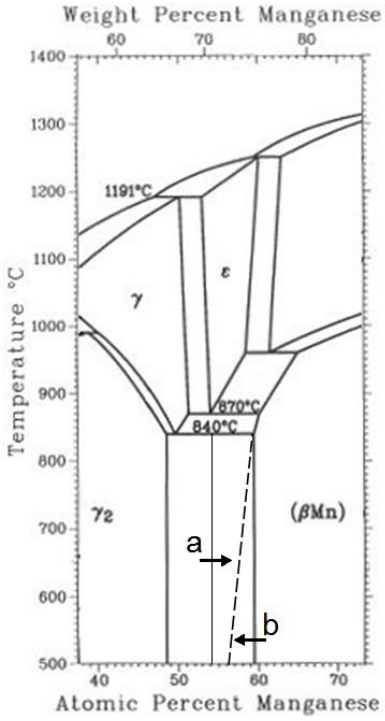

Figure 25 Magnification of Phase Diagram showing two-phase region where the τ-phase forms. a.) composition shift in the binary Al-Mn system, b.) change in phase diagram due to addition of boron.

3.1.4 Magnetic Properties

In the AS samples it is clear that there is a paramagnetic component as the slope is positive at the maximum applied field for all samples. Also it is interesting that there is no trend in magnetic properties in the AS samples and exhibit a low M_s. The ε-phase is undefined magnetically and although it has been proposed to be AF [27], here it clearly exhibits ferromagnetic behavior (Figure 26). The equilibrium phases have been assumed to be non-magnetic in the literature.

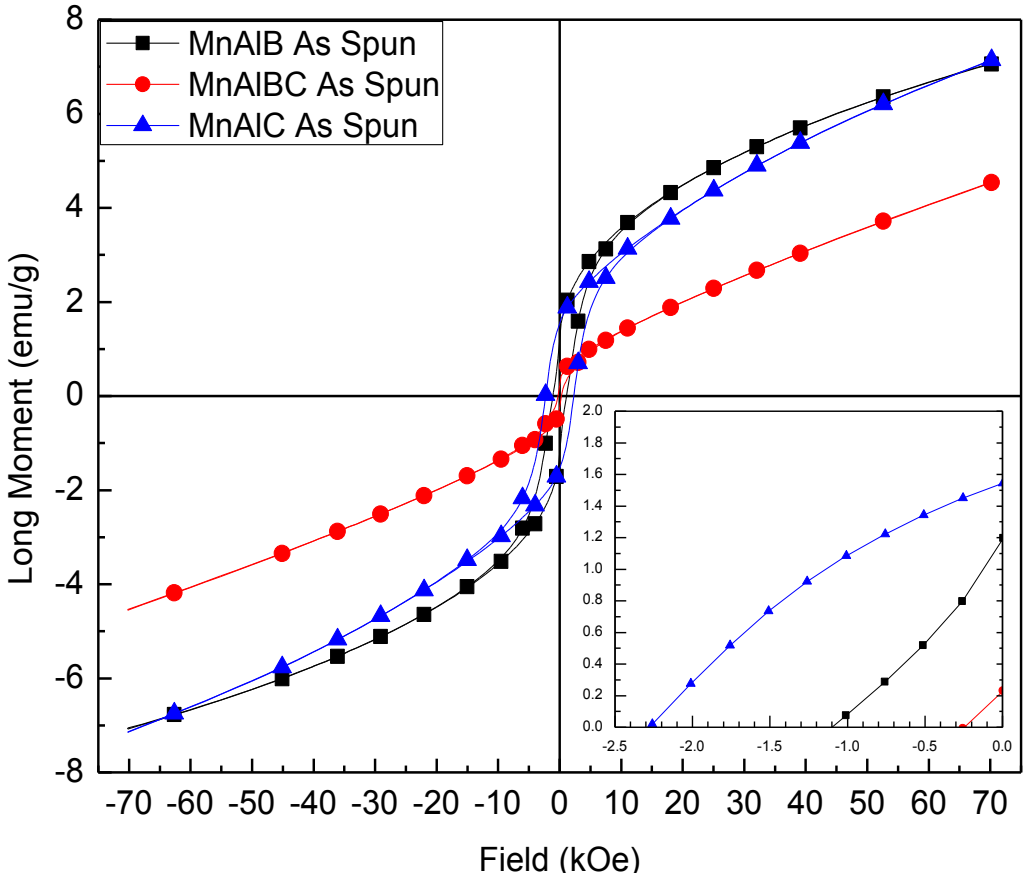

Figure 26 Room temperature (300K) hysteresis loops for AS samples with B, B-C, and C additions. Insert shows demagnetization curve more clearly. No trend is clear concerning either the magnetization or the coercivity with change of addition elements.

The shape of the hysteresis loops in the as spun samples (Figure 26) can be explained by a superposition of a FM phase and an AF phase. With the FM behavior owing to uncompensated spin pairs, potentially at the grain boundaries. This will produce similar effects to what has been suggested by [27] where there are multiple (AF and FM) ε-phases present in the as spun material but not necessarily at the grain boundary. The existence of two phases in the as spun material has been documented by both J.J. Van Den Broek et al.[22] and Yanar et al.[23] where the ε-phase remains the disordered AF phase and the existence of an ordered ε'-phase is prevalent in both reference and a homogeneous mixture exists. Either of these explanations is viable and both need further substantiation to be accepted. Furthermore, the saturation of such a sample (<10emu/g) renders the material novel at best although further management of the microstructure could lead to higher coercivity in the annealed state (e.g. introduction of AF exchange coupling) if some of the AF material can be retained.

With the annealed samples, it can be seen that there is a tradeoff between coercivity and magnetization with boron content. Figure 27 can be explained by the difference in microstructure; where the carbon (134.4 emu/g and 1.40 kOe) and carbon/boron (103.4 emu/g and 1.89 kOe) doped samples are almost pure τ-phase, the boron (47.5 emu/g and 2.42 kOe) -doped sample is less than 50% τ-phase. This reduces the magnetization but increases the distance between τ-phase grains which reduces the magnetostatic interactions and therefore increases the observed coercivity.

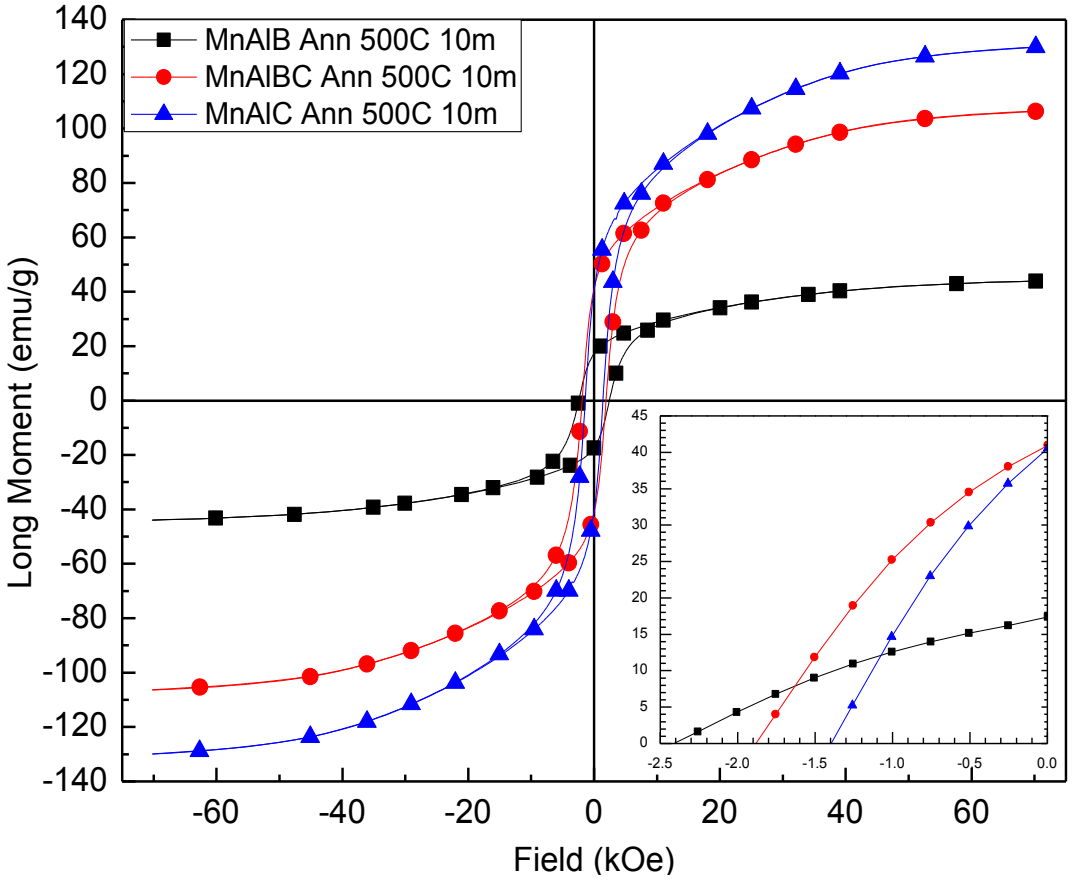

Figure 27 Room temperature (300K) hysteresis loops for annealed samples with B, B-C, and C additions. Insert shows demagnetization curves in detail. There is a tradeoff between coercivity and magnetization with change of additions.

Compiled in Figure 28 are the magnetic properties from the previous two sets of hysteresis loops consisting of AS and annealed samples of each of the three compositions. The magnetic properties of the as-spun samples show no trend with the change in composition, however there is a clear trend in the case of the annealed samples (Figure 28).

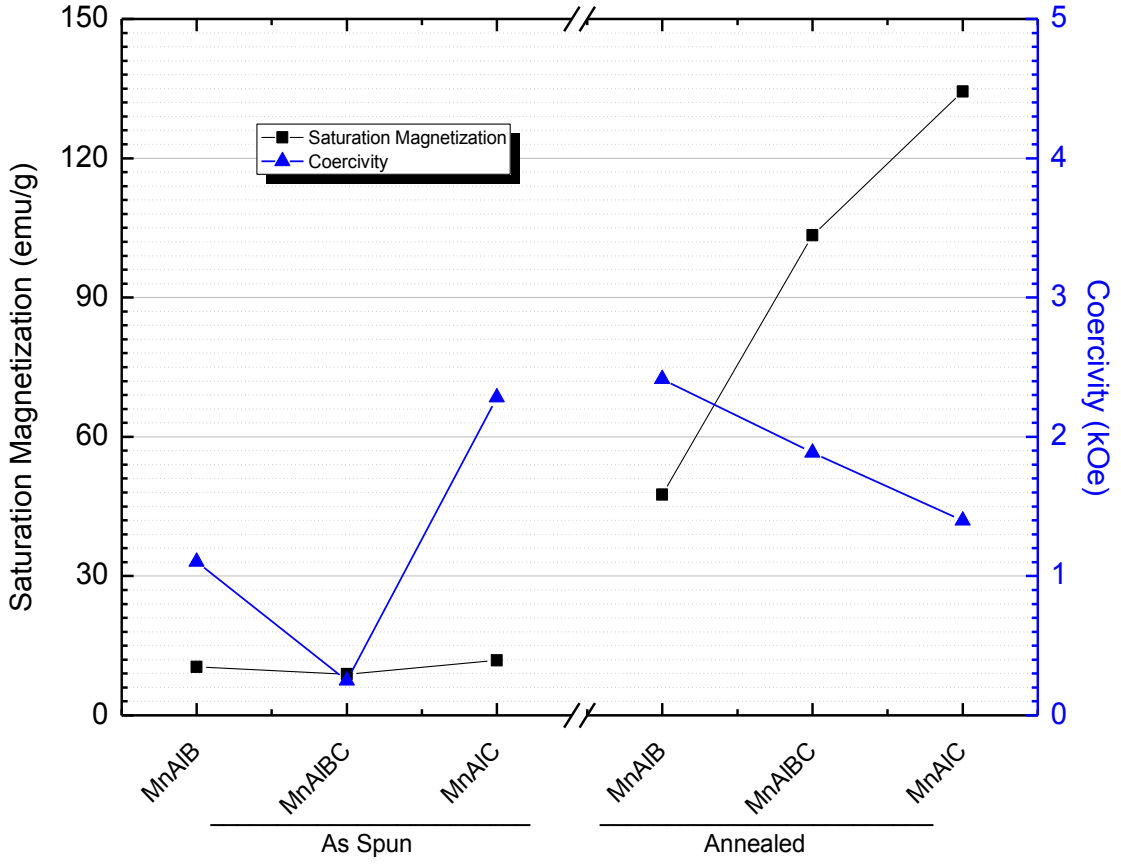

Figure 28 Magnetic properties of the B, B-C, and C samples in As-Spun and Annealed forms (all measured at 300K). The Annealed case shows a strong trend between the increase in Carbon content and the increase in saturation magnetization. Also the Coercivity decreases with the increase in Carbon content due to the ability of τ grains to interact in the phase pure carbon doped sample and its inability in the multi-phase boron doped sample.

The addition of carbon stabilized the ε-phase and therefore created samples with higher phase purity; this in turn increased the saturation magnetization but decreased the coercivity of the samples. The reasoning behind this trend is that with more τ-phase there is more magnetic material per gram and therefore the saturation increases, however with more τ-phase grains closer together their influence on each other is also increased. This

coupling effect is reversed with the addition of equilibrium phases as the physical separation of the τ-phase grains, by the equilibrium phase grains, decouples them and reduces the magnetostatic interactions. And, this is exactly what is seen in Figure 28; the boron-doped sample exhibits high H_c and low M_s which is expected from the XRD pattern. When looking at the boron and carbon-doped sample it exhibits a mixture of properties from the purely carbon or boron doped samples. This mixture of properties was further studied with a sample of $Mn_{54}Al_{44}B_1C_1$ (Batch 1 from Figure 21) at different annealing temperatures and durations. A spectrum of annealed samples can be seen in Figure 29 with AS and pure τ-phase references. It is apparent from this study that the optimal temperature for τ-phase formation is around 600°C. However, the transition to the τ-phase is diffusion governed and temperature and time has a similar effect on such processes. Therefore, samples were annealed at 600°C for longer durations (Figure 31).

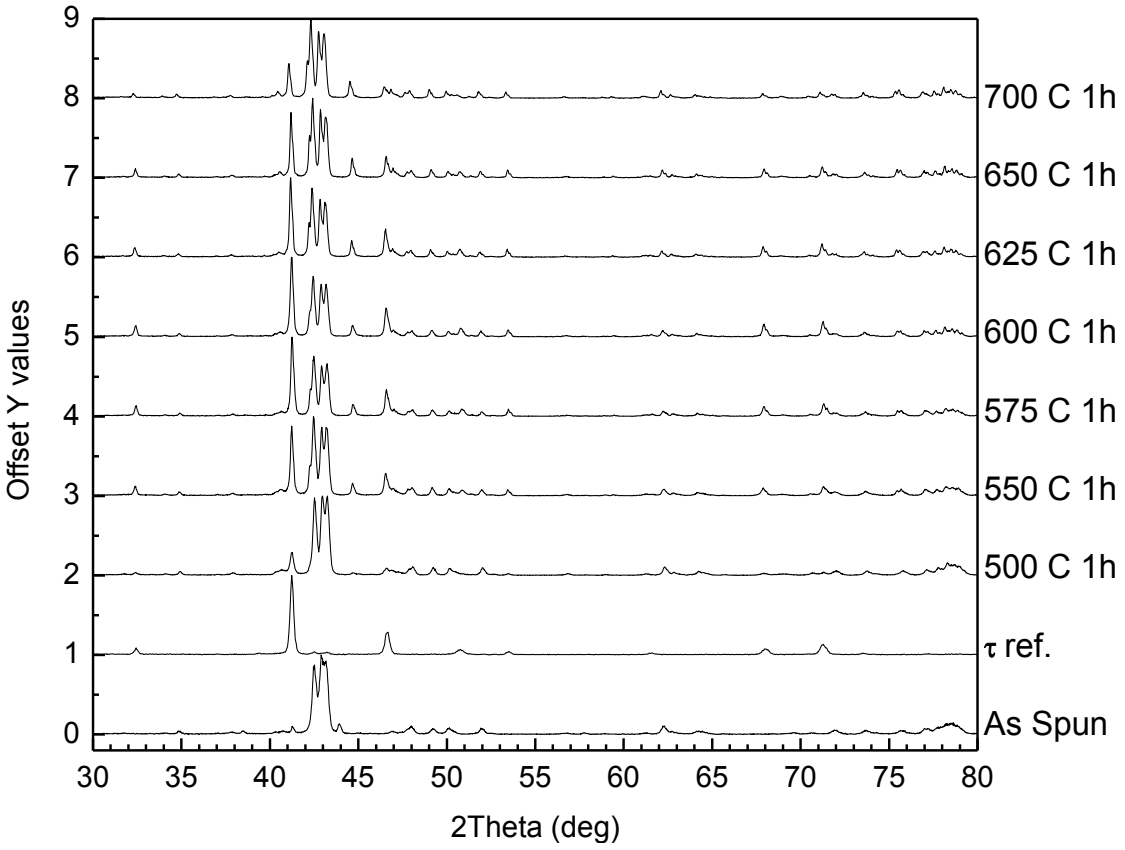

Figure 29 $Mn_{54}Al_{44}B_1C_1$ Annealed at different temperatures with a reference of pure t-phase.

The magnetic measurements for these samples were taken on an AGFM which as previously mentioned does not consistently measure the M_s, therefore the only magnetic property that will be reported for all samples is the coercivity (Figure 30). As can be seen, there is a large increase in H_c after initial heat treatment at 500°C and it continues until a plateau at about 600°C and then an eventual decrease above 650°C. The trend in H_c from Figure 30 can be observed directly in the XRD patterns of Figure 29 if the ratio of the highest τ-phase peak to the highest equilibrium phase peak is defined (left y-axis in Figure 30).

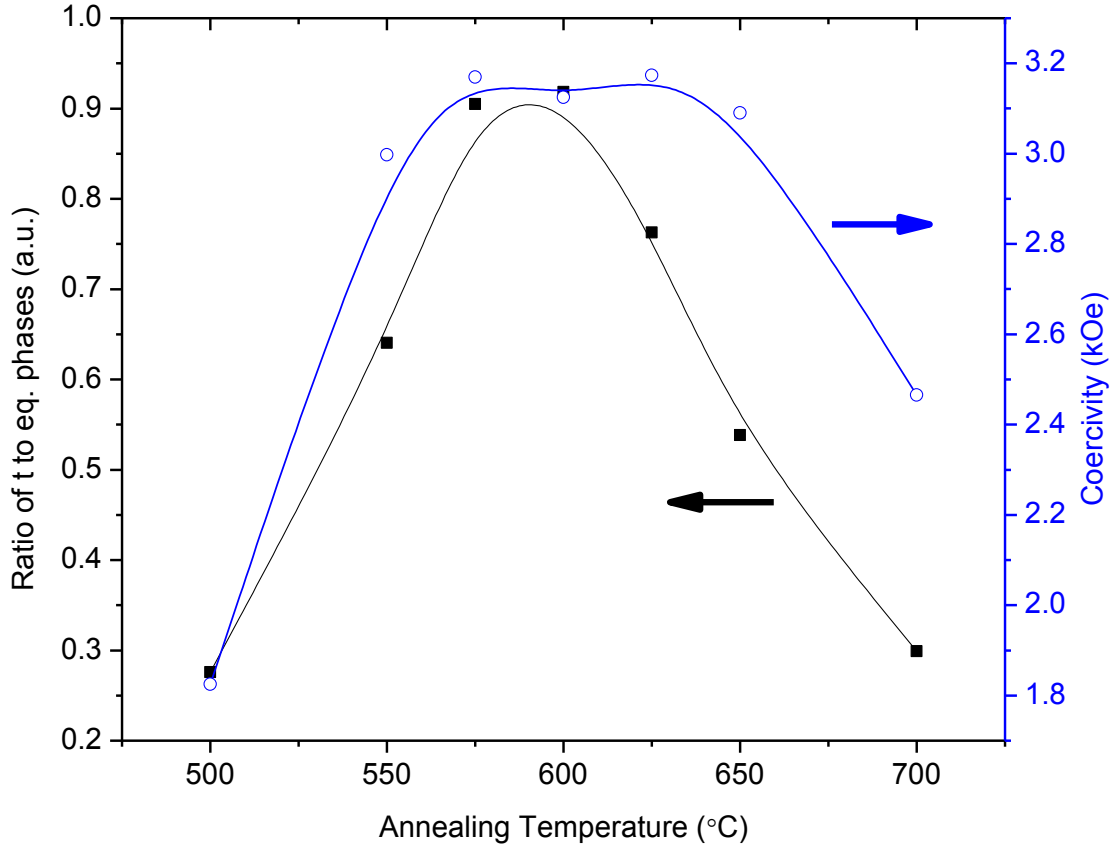

Figure 30 Coercivity of $Mn_{54}Al_{44}B_1C_1$ samples at various annealing temperatures (1 hour duration) with ratio of τ-phase to eq. phases from XRD (Figure 29).

Phase transformations, especially diffusion-driven ordering like the $L1_0$ structure, require time and energy; for this reason samples of $Mn_{54}Al_{44}B_1C_1$ were annealed at the optimum temperature of 600°C for longer durations to determine if this would increase the percentage of τ-phase in the alloy. Unfortunately, as can be seen in Figure 31 the increased duration only increases the percentage of equilibrium phases present in the alloy and does not foster the continued formation of the τ-phase. However, this turns out to be a desirable outcome in terms of the coercivity as the sample annealed at 600°C for 2

hours exhibited a coercivity of 3.2 kOe (Figure 32 and Figure 33), the highest reported coercivity for a sample after only heat treatment.

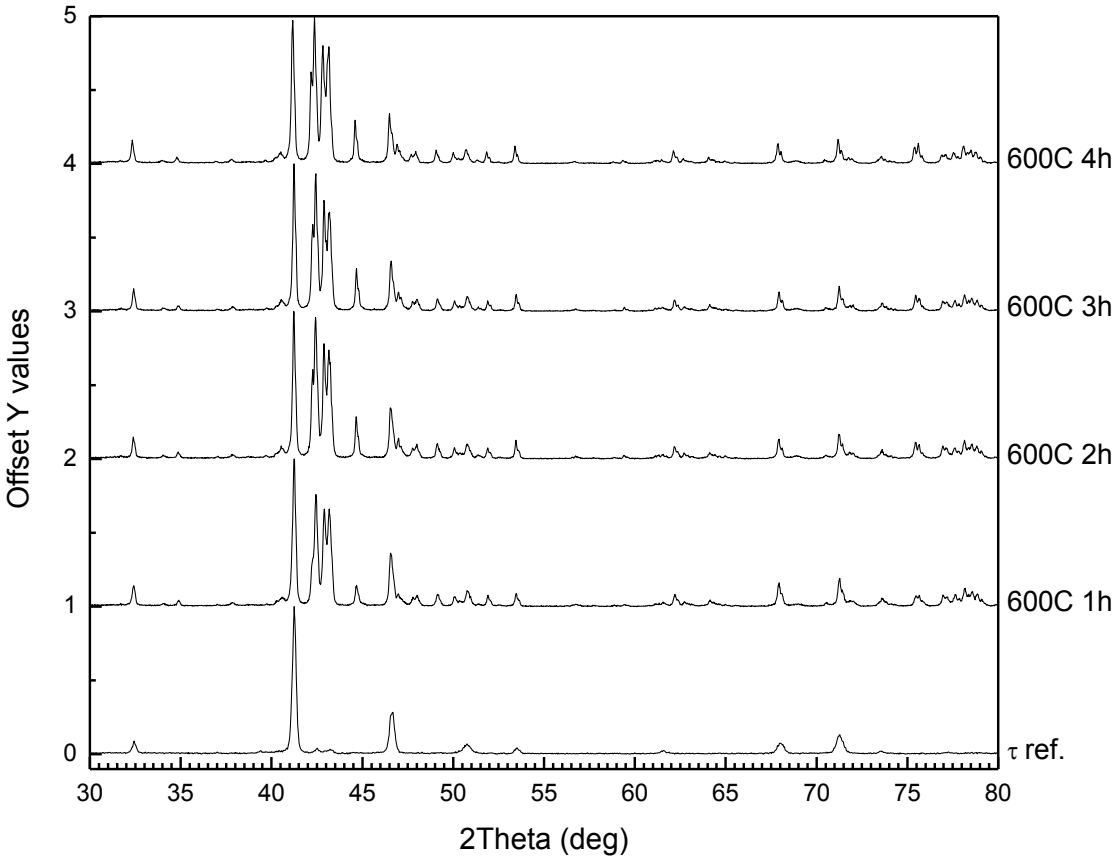

Figure 31 $Mn_{54}Al_{44}B_1C_1$ Batch 1 annealed at 600C for 1 to 4 hours. Sample exhibits growing equilibrium phase(s) with increased duration.

When annealing this specific sample for longer times, there is no appreciable increase or decrease in coercivity observed through the AGFM. This could be due to the small change in the ratio of τ to equilibrium (eq.)-phases from 2 to 4 hours of annealing. The coercivity increase is due to decoupling by eq.-phases that separate the FM τ-phase grains. There seems to be a loosely correlated inverse relationship between the ratio of τ to eq.-phase and the coercivity that can be seen more clearly in Figure 32. Again, this is

explained by the decoupling of the τ-phase grains by the equilibrium phases; however, the decrease in M_s is apparent in Figure 33 with decrease in phase purity.

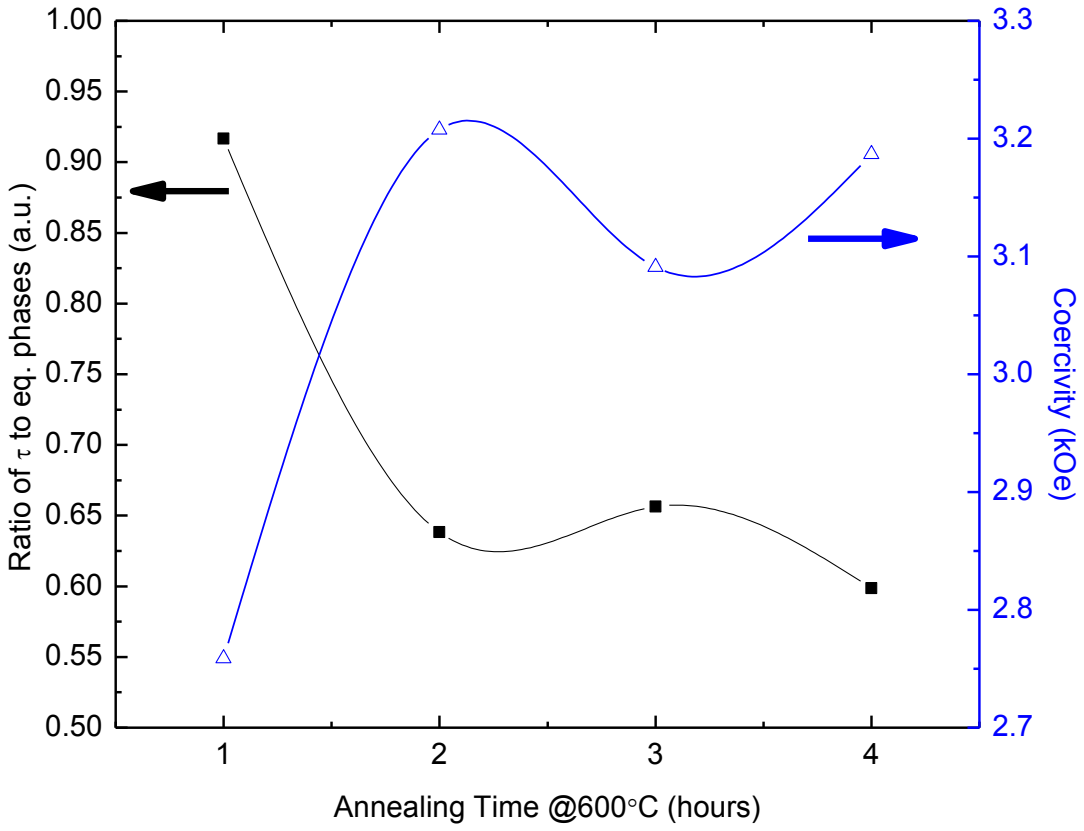

Figure 32 Coercivity of $Mn_{54}Al_{44}B_1C_1$ samples at various annealing times (at 600°C) alongside the ratio of τ-phase to eq. phases. An inverse relationship is apparent between the two values.

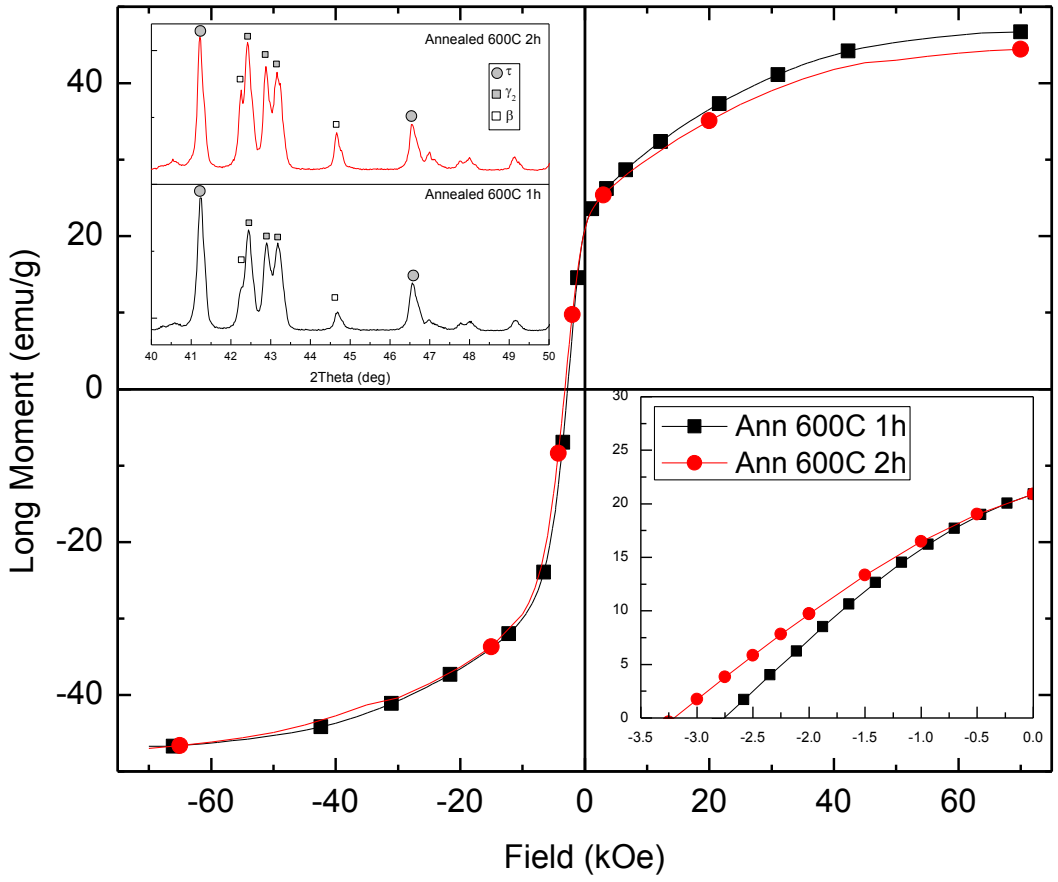

Figure 33 Highest coercivity samples of Mn54Al44B1C1, as can be seen with minimal heat treatment coercivities of around 3.2 kOe can be achieved for this system. Inserts show demagnetization curves (lower right) clearly showing M_r and H_c and XRD close-up (upper left) showing relative amounts of various phases for the same.

Overall, the addition of boron does not aid in the formation of the τ-phase; in fact it seems to reduce the stability of both metastable phases and augment the formation of the γ_2-phase upon cooling. The preferential formation of one over the other when it comes to the two equilibrium phases has been proposed to be a compositional preference; however the β-phase seems to form regardless of boron content suggesting a change in the phase diagram. Alternatively, the addition of boron could be used to intentionally retain some

equilibrium phase which would increase the coercivity (at a cost of magnetization) without time-consuming post-processing. The long-term stability of the boron doped samples has yet to be determined, but is expected to be less than that of the carbon doped samples. However, a combination of boron and carbon could prove to increase the coercivity and the stability of the material.

3.2Mechanical Milling (MM)

Mechanical Milling and Mechanical Alloying (MA) have been employed to create nano-sized crystalline features (grains, defects, etc.). Mechanical Milling begins with a homogeneous material, whereas Mechanical Alloying uses the high energy ball milling (HEBM) process to create a homogeneous mixture of two or more elements. MA starts with two separate elements and mixes them together, whereas MM starts with a well defined alloy and reduces the particle size (sometimes to that of a single grain or in this case, magnetic domain). First, it is necessary to create a preliminary alloy with the highest possible magnetic properties. To do this it is helpful to look at the XRD patterns of two compositions of carbon-doped Mn-Al alloys (Figure 34) as the purity of the parent ε-phase directly affects the magnetic properties as previously shown.

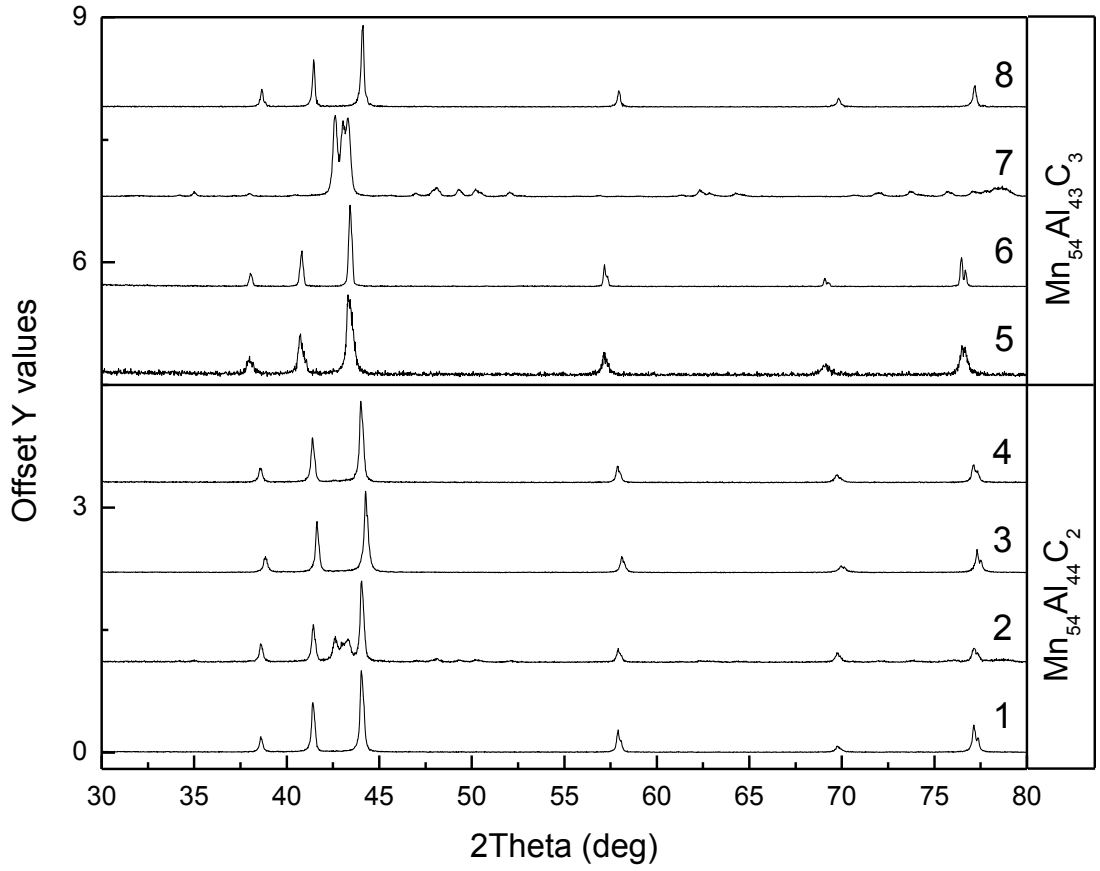

Figure 34 Different batches of Mn-Al-C with composition 54-44-2 on bottom and 54-43-3 on top. The higher percent of carbon is thought to increase both the magnetic properties and the phase purity.

Mechanical milling is carried out on the samples that show the highest phase purity to try to increase the magnetic properties of the Mn-Al system. Therefore, for the purposes of this study the composition of $Mn_{54}Al_{43}C_3$ will be used as it has exhibited the best magnetic properties in literature[13,21]. Batch 6 (above Figure 34) was used to carry out MM in a nonreactive gas atmosphere, while batch 8 was used for surfactant assisted MM.

3.2.1 Nonreactive Gas Milling (NGM)

The annealed batch 6 was milled in 1 hour increments until it was clear that amorphous material was being created; this happened after only 3 hours as can be seen in the XRD patterns (Figure 35). Also, based upon the magnetic properties milling at smaller increments (10 minutes) was carried out until the preliminary optimum time of 1 hour (Figure 35). The results of such a milling regime are rather characteristic of mechanical milling, peak width increase due to grain size decrease to the nano-scale.

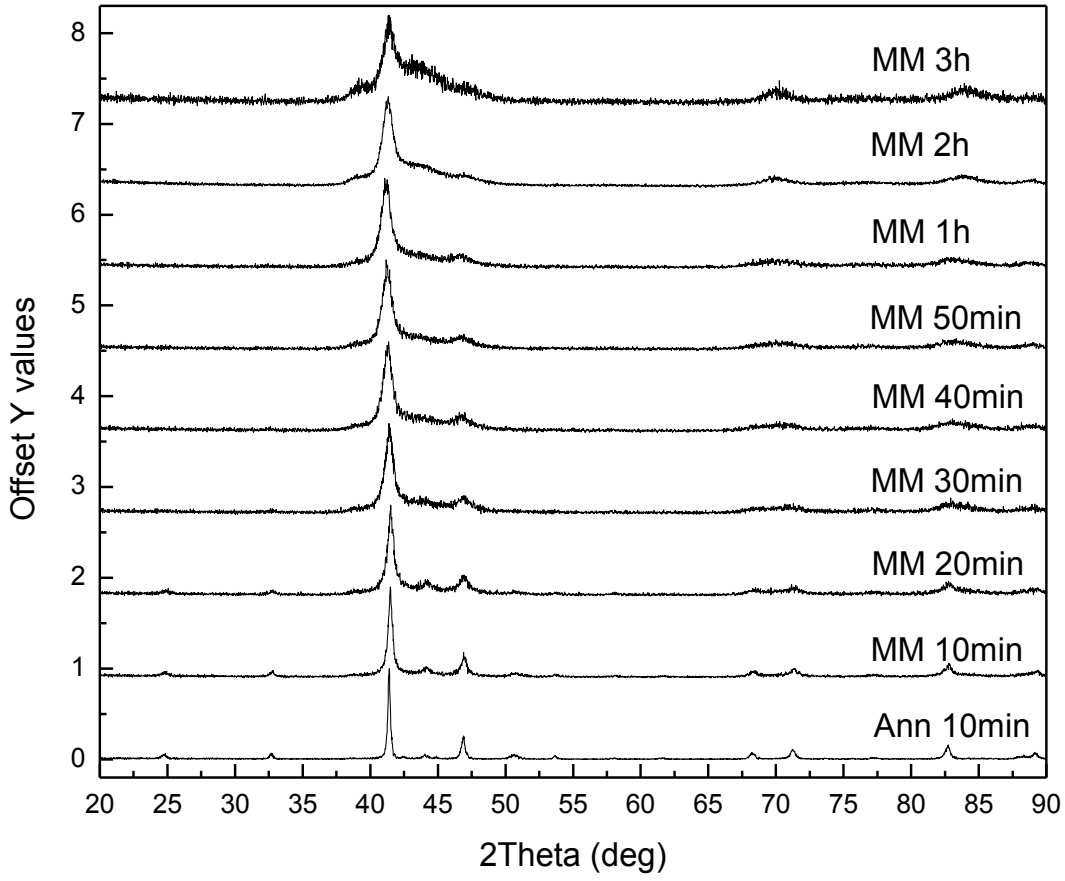

Figure 35 Mechanically milled samples from Annealed Batch 6 Mn54Al43C3. Note peak broadening after only 30 minutes of mechanical milling and broad amorphous peak around 44° 2θ.

From the XRD patterns it is clear that there is a large increase in the peak width after only 20 minutes of milling. Unfortunately, there is an increase in the equilibrium phase peak cluster (small group of high intensity peaks all from the γ_2-phase at about 44° 2θ in Figure 35) from the annealed sample throughout milling although most notably before the peaks converge at 30 minutes of annealing. At which time a broad diffuse peak begins to appear in the same region, suggesting amorphization of the material.

When the hysteresis loops are analyzed for the samples milled at 1 hour intervals (Figure 36) it is clear that there is a large increase in the coercivity after only 1 hour and a decrease thereafter. The maximum for magnetic properties being at 1 hour is interesting to Also, the loop for the 3 hour milled sample exhibits a “wasp-waisted” quality that is characteristic of a two-phase system. This suggests that there is a large proportion of either amorphous material or another phase (e.g. γ_2) being formed at this point which is substantiated by the XRD patterns in Figure 35.

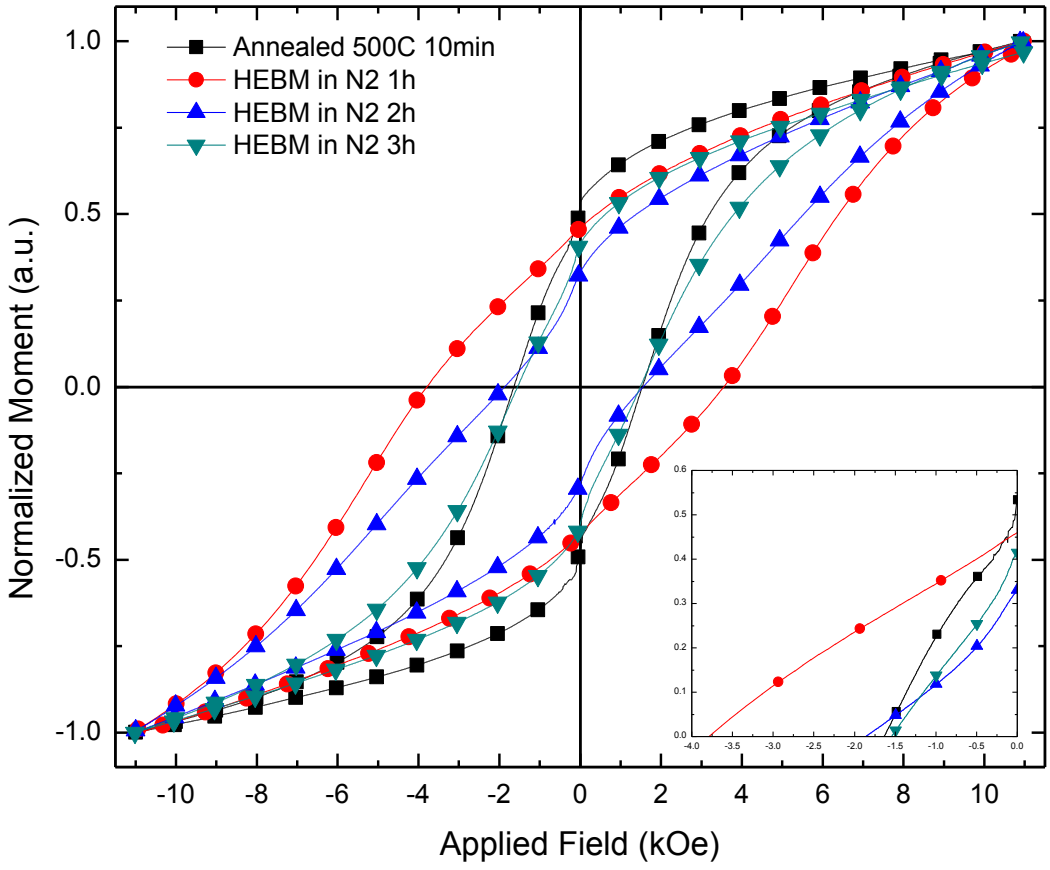

Figure 36 Normalized hysteresis loops (AGFM) for preliminary milling study (1h increments until 3 hours). Notice large increase in coercivity from annealed sample to 1h milled sample and decrease after 1h as well as two-phase nature.

Also, the transition from the hard magnetic phase present in the 1h milled sample to the relatively soft phase apparent in the 3h milled sample can be viewed directly in the form of the 2h milled sample. The M_s cannot be measured from these loops therefore the first few samples were re-run in the SQUID magnetometer (Figure 38). Again, it is interesting to note the tradeoff between coercivity and saturation magnetization in the SQUID-measured samples in Figure 38. After this preliminary study the same procedure was

done for 10 minute intervals between 0 and 60 minutes to determine the drop off point of the increase in coercivity.

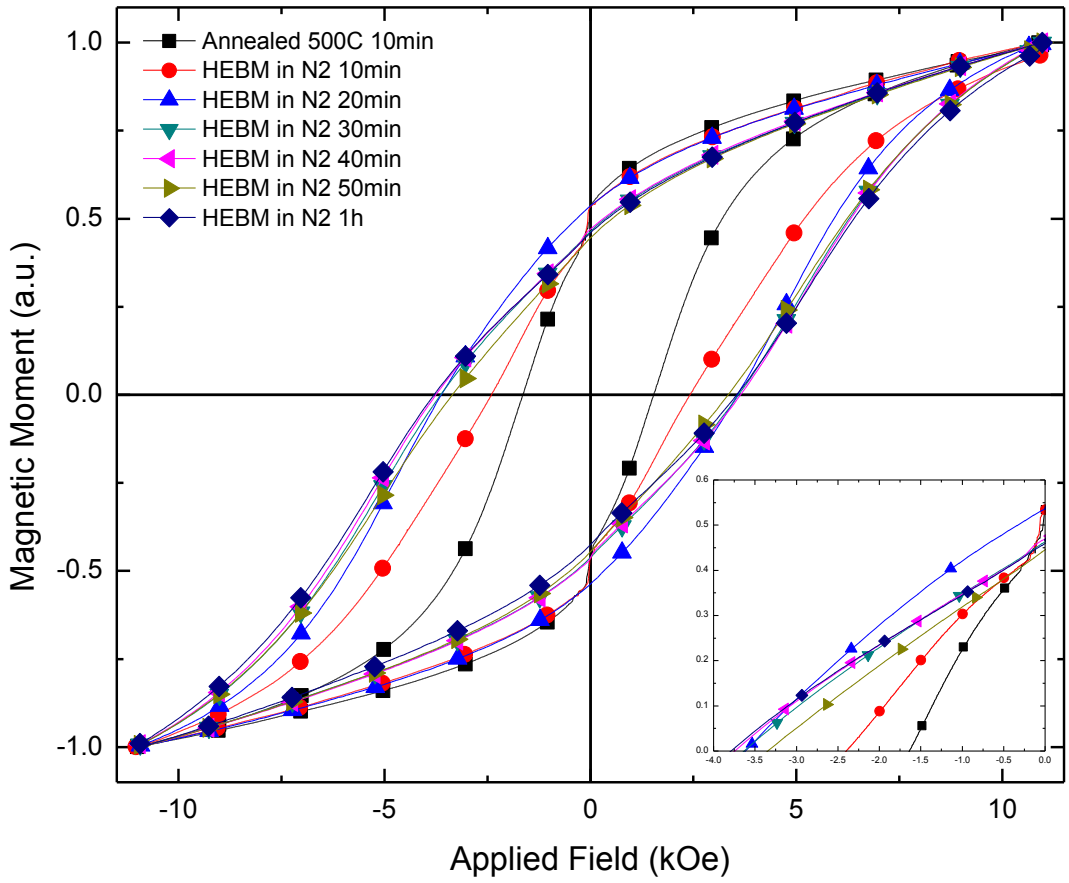

Figure 37 Follow-up magnetic study of milling times up to 1 hour with insert of demagnetization curve showing coercivity. Note H_c increases to a maximum of 3.9 kOe at 1 hour.

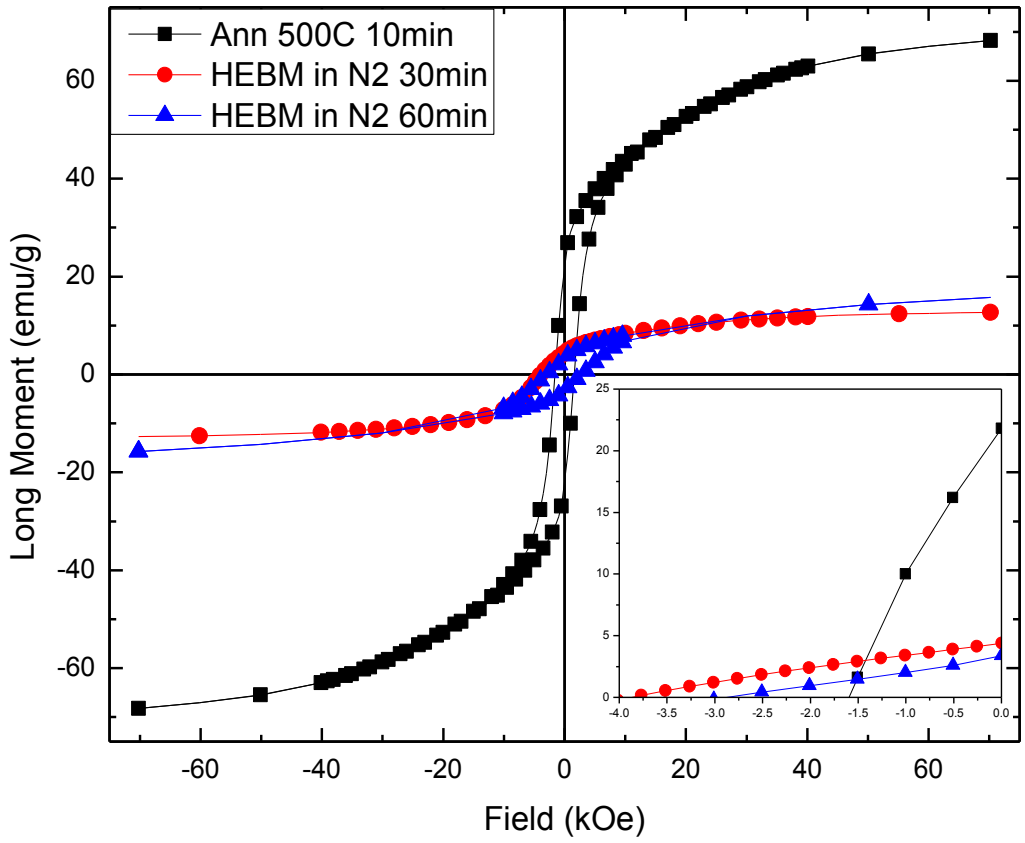

Figure 38 SQUID Magnetometer measured hysteresis loops showing the large increase in coercivity and tradeoff for saturation magnetization.

The SQUID measured hysteresis loops tell a different story than those measured by AGFM, namely that the sample milled for 30 minutes exhibits a large coercivity of 3.88 kOe, and the sample milled for one hour has a smaller coercivity of 3.53 kOe. Unfortunately, for both cases the magnetization is very low (less than 20 emu/g) confirming the loss of τ-phase, possibly in favor of equilibrium phases or amorphous material. The magnetic properties of these samples have been compiled in Figure 39 for both SQUID and AGFM (adjusted and not adjusted) measurements. The SQUID data exhibits a trend that is characteristic for this study, namely a tradeoff between M_s and H_c

after only 30 minutes (and possibly less) of milling time. The drastic decrease in M_s for this processing technique implies that a change in fabrication procedure is needed to retain the high M_s of the material while increasing the H_c. The change in H_c between adjusted and not adjusted AGFM data is descriptive of the adjustment process. The subtraction of a paramagnetic line from the hysteresis loop shifts the left side up and increases the coercivity.

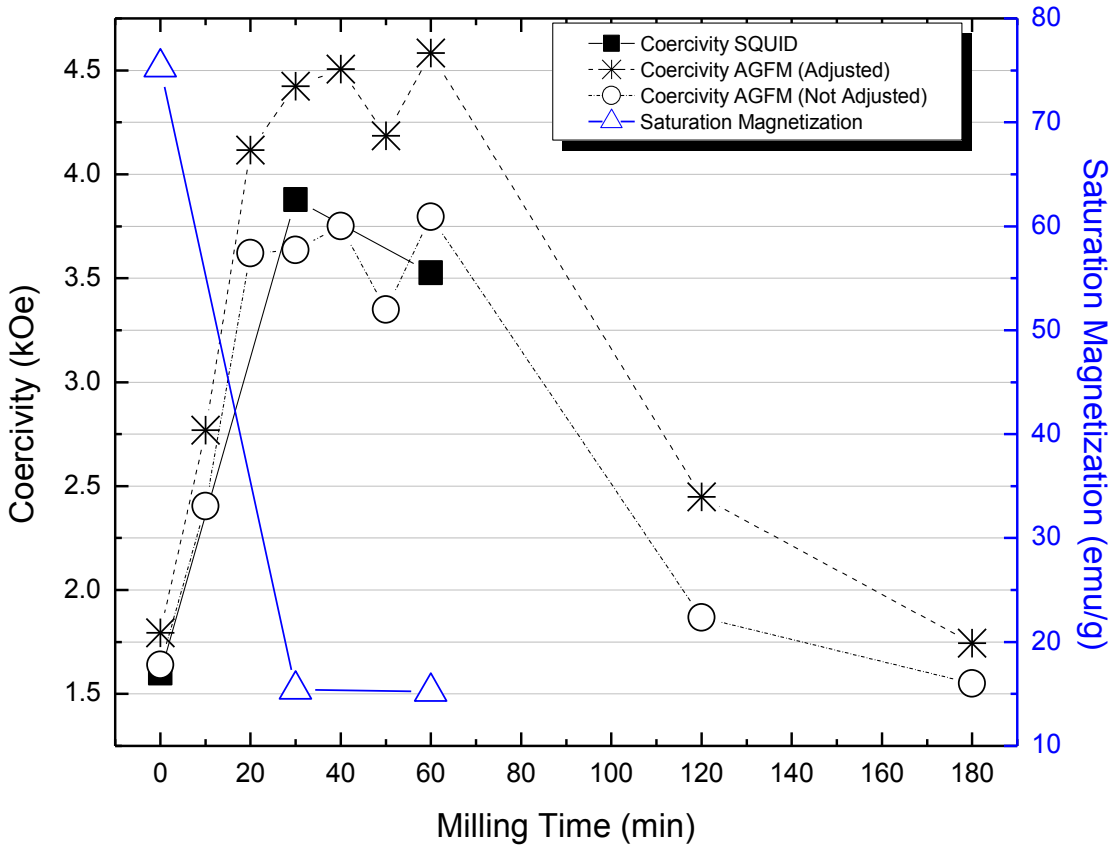

Figure 39 Magnetic Properties of HEBM samples in Nitrogen gas showing the same tradeoff between coercivity and saturation after only 30 minutes of milling. Notice difference between SQUID data and AGFM data as well as difference in trend between adjusted and non-adjusted AGFM coercivity data.

The drastic loss of saturation must be addressed before this material (and more specifically this fabrication procedure) can be used as a permanent magnet processing route commercially. One possible method of saturation reduction is oxidation. During the milling process any amount of oxygen sealed within the vial can be incorporated into the material as it is a high-energy deformation process. Energy dispersive x-ray spectroscopy was performed on the milled samples (every 1h increment) and the oxygen content was calculated and presented in Figure 40. It is clear that there is a large amount of oxygen contamination after 1h of milling; however, this can be alleviated by being more cautious when sealing the vial, and possibly by using a newer style of vial (only one open end). The presence of oxygen in amounts seen here could reduce the saturation by creating compounds of MnO $Mn_2O_3$and Mn_3O_4 which are mostly PM, ferrimagnetic, and PM respectively, all of which would have a significant effect on reducing the saturation value. Another mechanisms for saturation reduction include Mn vaporization due to the low vapor pressure of Mn and the high energy nature of the milling process coupled with the heat generated during the milling (although measures have been taken to reduce the increase in temperature during milling). Furthermore, the large amount of energy transferred to the material by the process can manifest itself in defects of all kinds and if anti-site defects or stacking faults are introduced the distance between nearest neighbor Mn atoms could be reduced enough to encourage AF exchange coupling which increases the H_c but decreases the M_s.

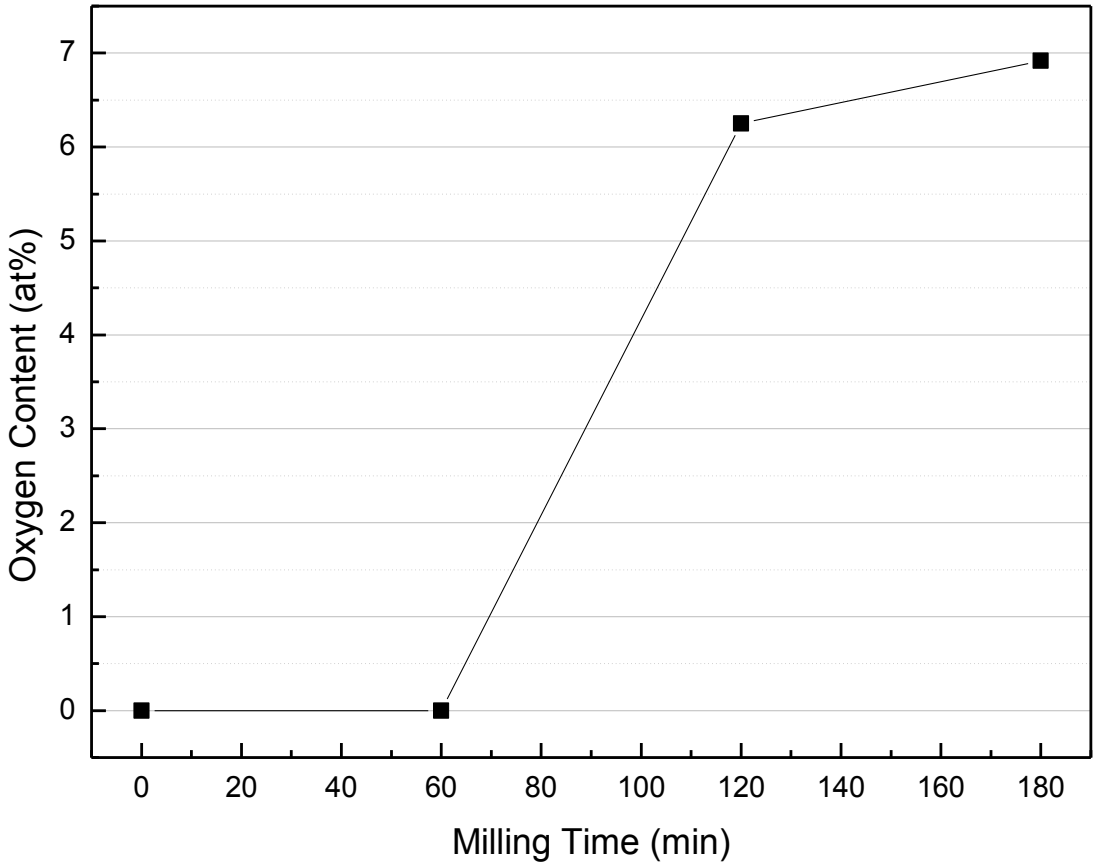

Figure 40 EDX results for O2 content versus milling time. Large amounts of oxygen present after 2 hours of milling (possible contamination).

Another interesting trend to notice is the grain size vs. coercivity of the milled samples (Figure 41). The trend follows roughly as outlined previously [1] where the single domain limit is approximately 20nm, after which the coercivity begins to drop off. However, the drop off can also be due to amorphization of the sample leading to a multi-phase system for which the previously discussed trend does not account. If this trend is to be followed it must be for more single-phase samples than present here.

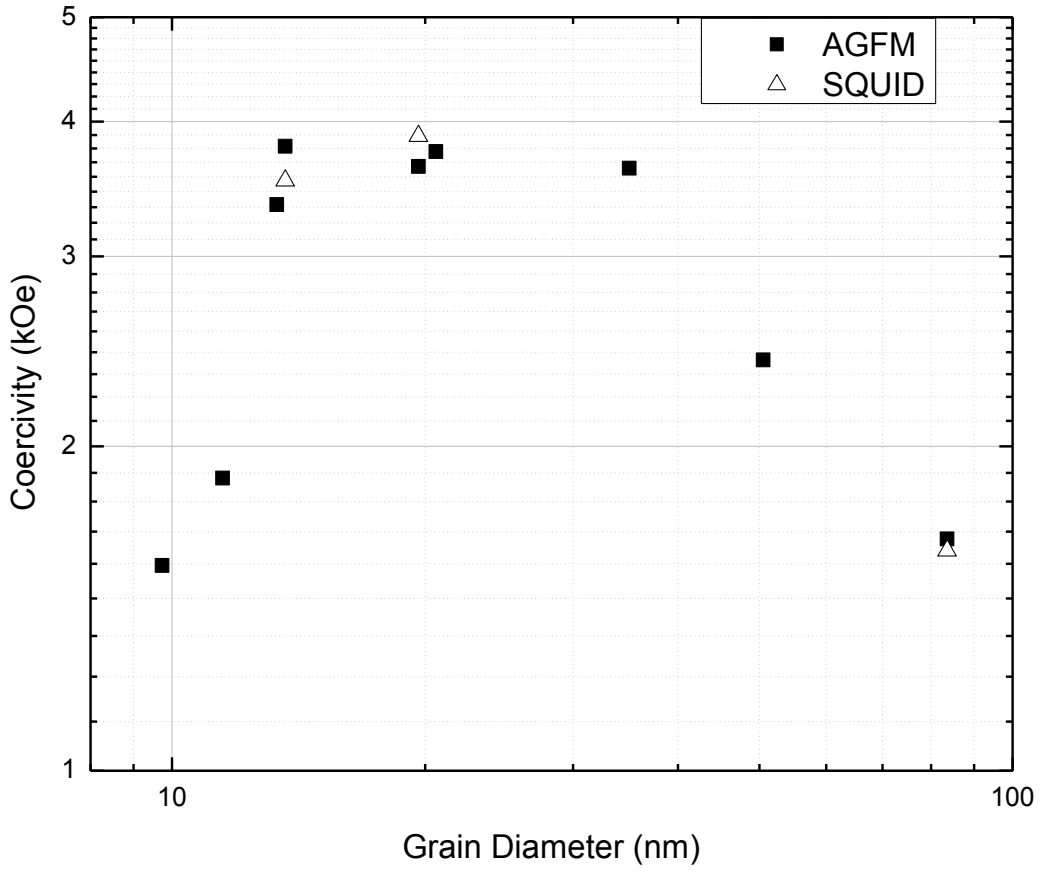

Figure 41 Grain size vs. coercivity following single domain limit outlined in Introduction. Showing results for both AGFM and SQUID tests.

In the end, high energy ball-milling of Mn-Al alloy should be carried out cautiously as the magnetic τ-phase is very shape specific. If antisite defects are introduced in the form of Mn in the Al layer, or entire layer shifts (ABAB to ABBA) by deformation then the Mn nearest neighbors will couple antiferromagnetically and drive down the saturation. One possible method of milling that could help reduce the effects of this problem is surfactant assisted mechanical milling. The surfactant would act as a buffer to keep the manganese from vaporizing and keep the individual grains from reforming (which drives

down the H_c). However, introducing more variables to the fabrication process increases the complexity and the possibility for error and should be performed carefully.

3.2.2 Surfactant Assisted Mechanical Milling (SAMM)

The milling times for SAMM were chosen based upon other studies with similar materials, and as the XRD patterns below (Figure 42) follow a similar development as the NGM samples it is expected that the grains approach nano-scale after only 30 minutes of milling. The lack of large peaks around 44° 2θ (except for the sample milled for 10 h) suggests that the formation of equilibrium phases is reduced with the use of a surfactant.

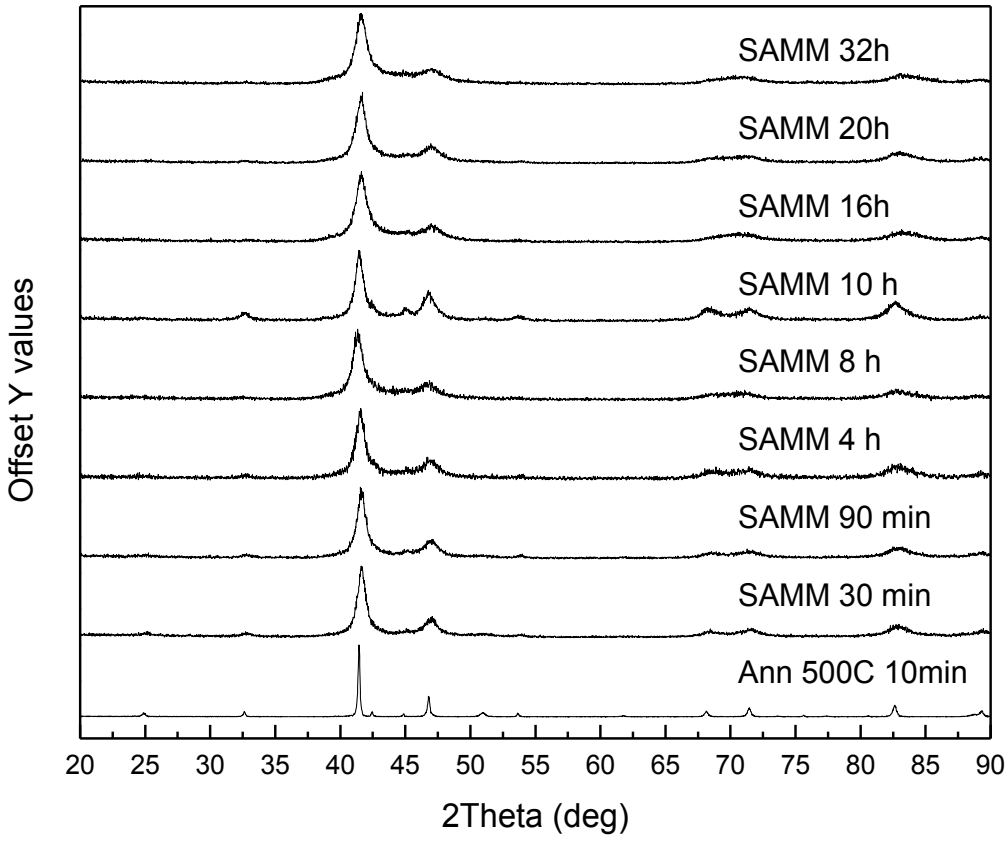

Figure 42 XRD patterns for SAMM samples at various milling times.

All milling times exhibit the same tradeoff between H_c and M_s; however, there is no paramagnetic or two-phase behavior. This suggests that the surfactant is doing its job and keeping the grains from re-welding as well as keeping them intact (not forming amorphous material). Unfortunately though, the M_s suffers as a result of milling for a number of possible reasons: the destruction of the τ-phase (in favor of equilibrium phases) or partial cleaning of the samples after contact with surfactant. The destruction of the τ-phase can be measured with XRD and aside from the 10h sample there is little evidence for the formation of other phases, but all samples exhibit a subtle amorphous peak centered between the (111) and (200) peaks for the τ-phase at 41.5 and 46.8 °2θ respectively. The partial cleaning of the samples can be measured with a TGA which measures the mass of the sample continuously throughout a temperature range. Oleic acid has a flash point of 360°C; therefore, heating the sample from RT to 400°C should remove any residual OA and should be visible on a TGA graph.

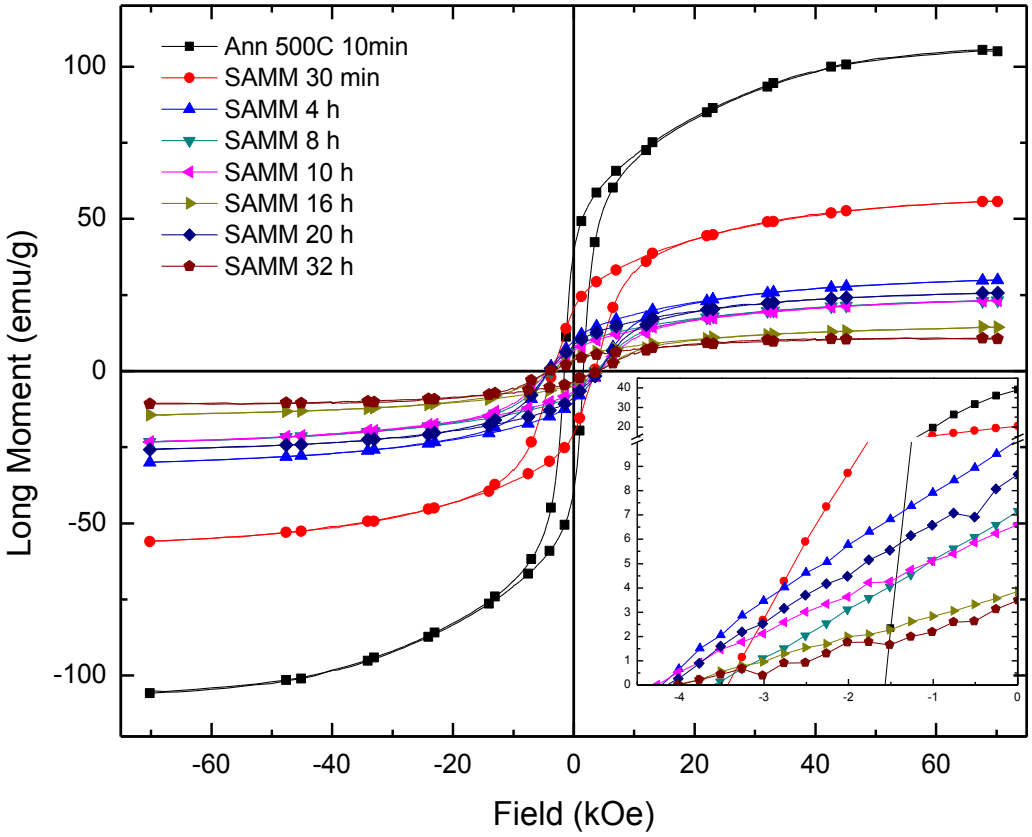

Figure 43 Hysteresis loops for SAMM samples. Notice drastic increase in coercivity until one hour and continued decrease in saturation after one hour.

There was no variation in mass throughout the RT (RT) to 400°C range suggesting that no significant amount of surfactant remained (Figure 44). Unfortunately this means that there is another factor that is driving the saturation down for these samples. One other possibility is that since the grains/particles are on the nano-scale the formation of any amorphous material could mean there is an AM coupling between the amorphous material and the FM grains. This could explain why there is such a drastic decrease in M_s since AF coupling would reduce the net magnetic moment for each grain.

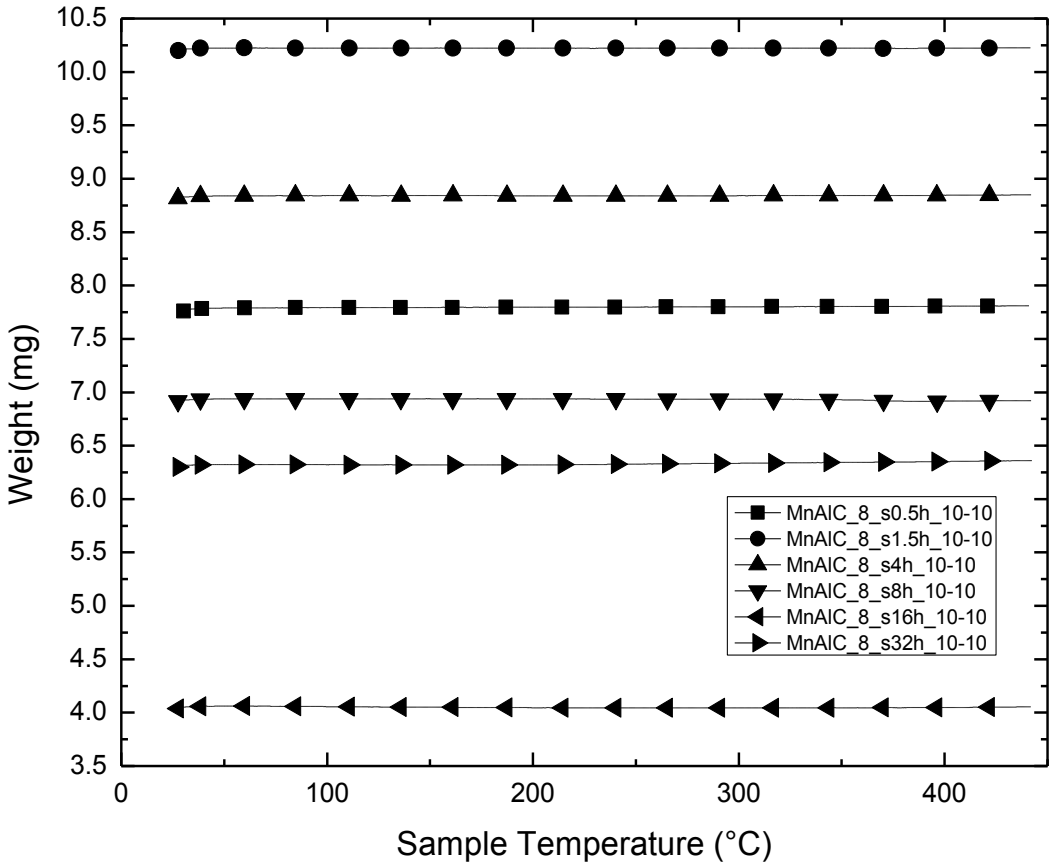

Figure 44 TGA curves for a number of SAMM samples. No variation in weight suggests a clean sample (no OA).

The tradeoff between H_c and M_s is apparent even for the SAMM samples; however there is no drastic drop off of H_c after a certain point (unless after 32h). Surfactant may be the cause for this lack of drop off in H_c because, as was shown by the XRD results, there is little production of other phases or amorphous material even at long milling times. This yields a maximum combination of H_c and M_s at around one hour which is similar to that of NGM. The highest coercivity reported in this study of 4.2 kOe is for the 4h SAMM sample which exhibits a M_s of 34 emu/g (significantly lower than the maximum theoretical value 144 emu/g for Mn-Al[24]).

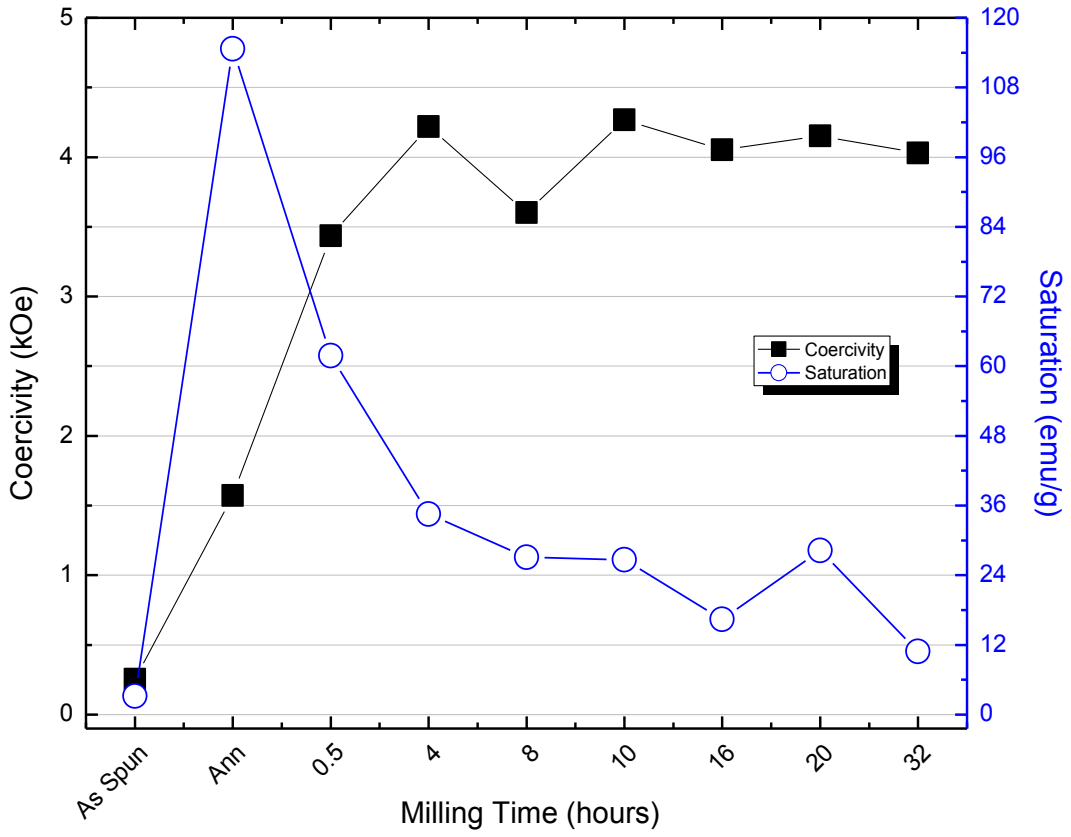

Figure 45 Magnetic properties of SAMM samples from AS to 23h of milling. Notice tradeoff between Hc and Ms and plateau of Hc with no dropoff after continued milling.

Once again, the grain diameter was calculated from the XRD peaks for each milling time and the results were plotted against coercivity (Figure 46) and a similar trend is observed. However, as may be assumed from the XRD patterns, after 4 hours of milling there is little to no difference in peak width. As summarized earlier the grain size calculations rely heavily on the peak width and therefore are a direct measure of the grain size. And, as the coercivity is directly related to the grain size a similar trend should, and is observed (Figure 45 and Figure 46).

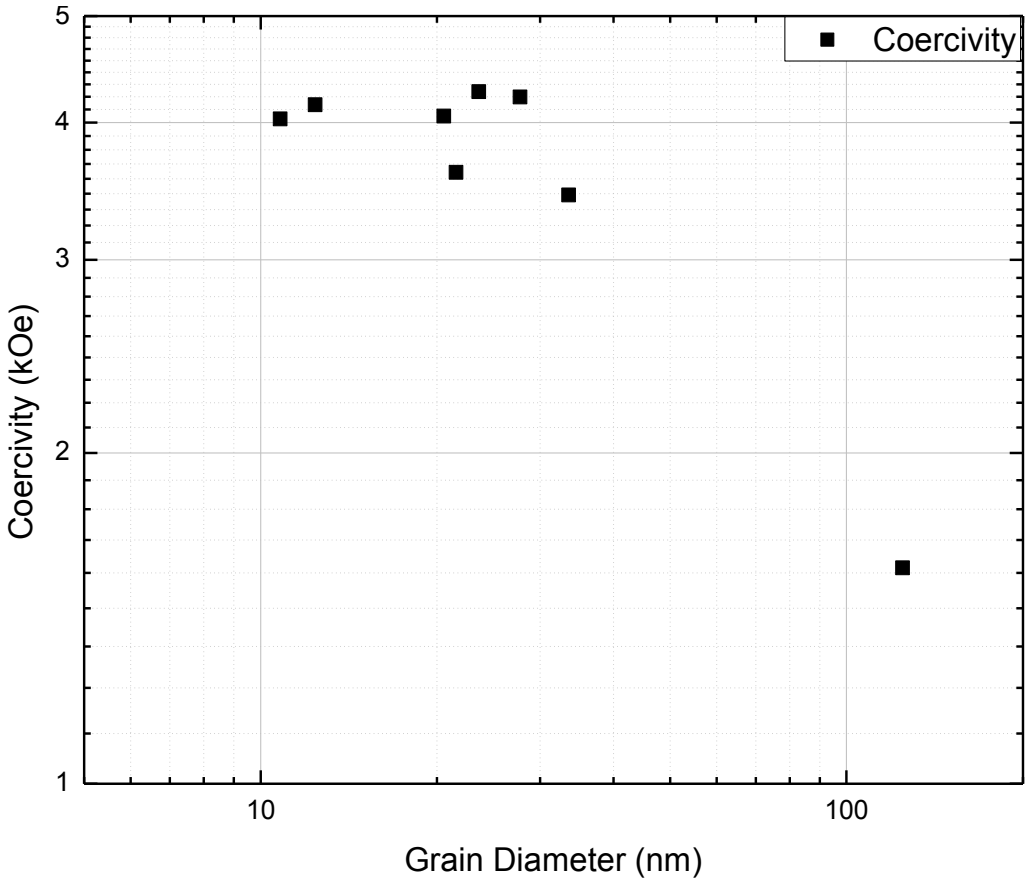

Figure 46 Grain diameter vs. coercivity for SAMM samples. All samples after 10 hours of milling the coercivity remained the same and there was little change in the XRD patterns and therefore little change in grain size.

SEM images were taken of samples at selected milling times for characterization and as can be expected from the previous results there is little difference that can be seen for all of the SAMM samples (Figure 47). However, when comparing the grain size for each sample, there is a small shift from 30 minutes to 32 hours, 34 to 11 nm respectively (Figure 47 i). A side-view of the "platelets" that have been formed can be seen in Figure 47 b with a thickness of about 3μm (measured elsewhere).

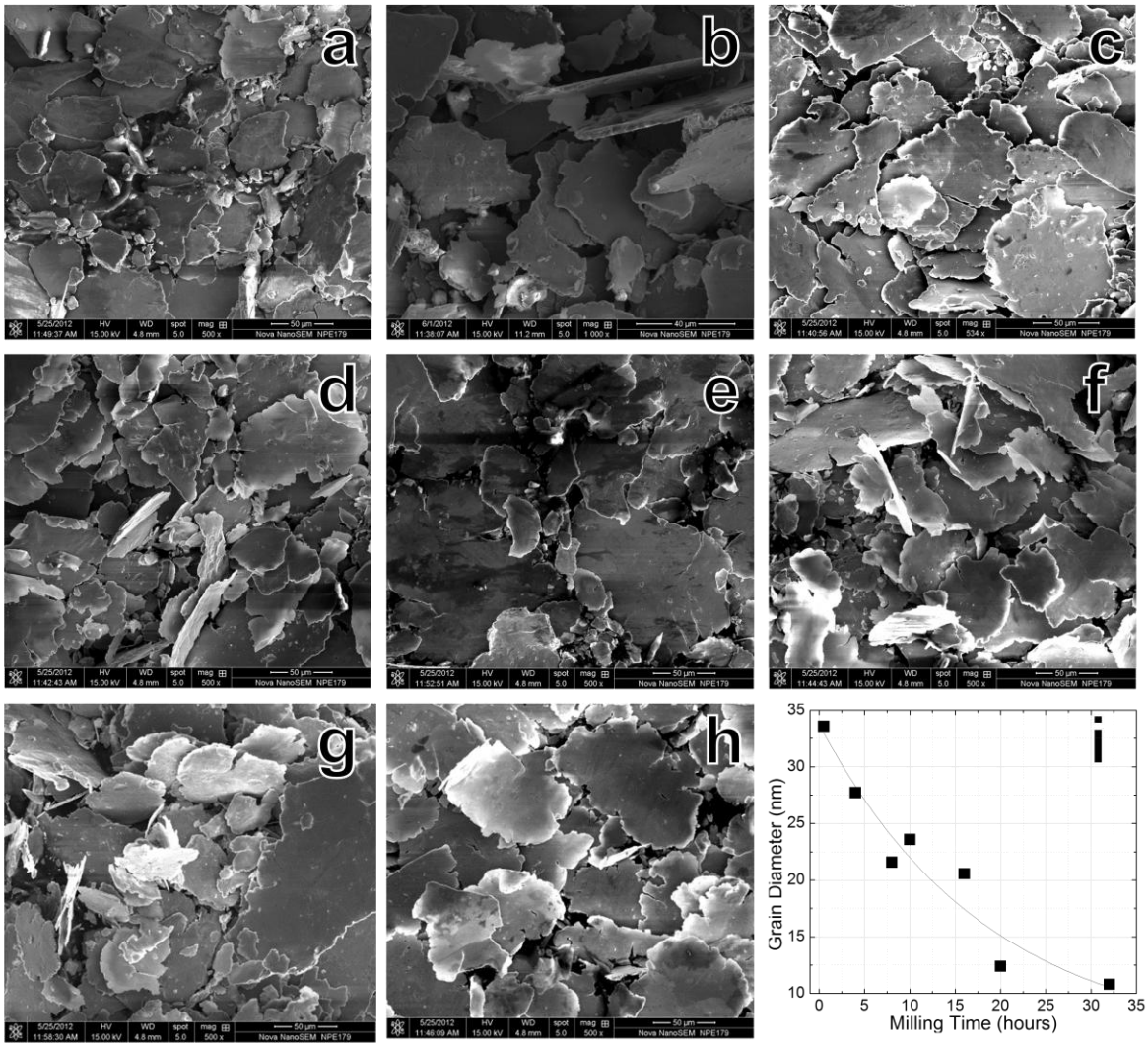

Figure 47 SEM micrographs of SAMM samples and grain size analysis. a.) 30 min scale bar 50µm b.) 90 min scale bar 40µm c.) 4h scale bar 50µm d.) 8h scale bar 50µm e.) 10h scale bar 50µm f.) 16h scale bar 50µm g.) 20h scale bar 50µm h.) 32h scale bar 50µm i.) Graph of grain diameter vs. milling time for all samples but (b).

From the SEM images it is clear that this approach to milling is having little to no effect on the re-welding of the particles, and after a certain point of milling there are no more gains to coercivity that can be measured. For this reason it is suggested that different

processing procedures be explored in the SAMM regime; as an example, varying surfactant type and ratio to powder, as well as varying milling medium amount. However, the tradeoff between M_s and H_c will be present whenever there is destruction of the magnetic phase (amorphization) and therefore cannot easily be avoided with HEBM.

3.3Literature comparison

It is interesting to compare the best values for this study with those from the literature directly. The tabulated values are displayed in Figure 48 with the bulk samples to the left and mechanically milled samples to the right. It is necessary to pay close attention to the composition of each alloy labeled below and the processing procedure for each. The results from this study are labeled with "Prost, Shield." Also, it is interesting that the annealing then milling process may be detrimental to the magnetic properties and the opposite should be tried for these compositions. The hope was that the surfactant would reduce the detrimental effects of HEBM, however, the results from this study suggest otherwise. With the theoretical value of M_s being calculated as 144 emu/g for the Mn-Al system[24] it is exciting to have a sample display an M_s of 134 emu/g experimentally ($Mn_{54}Al_{44}C_2$). Unfortunately, this sample's Hc was relatively low (1.39 kOe) for this system.

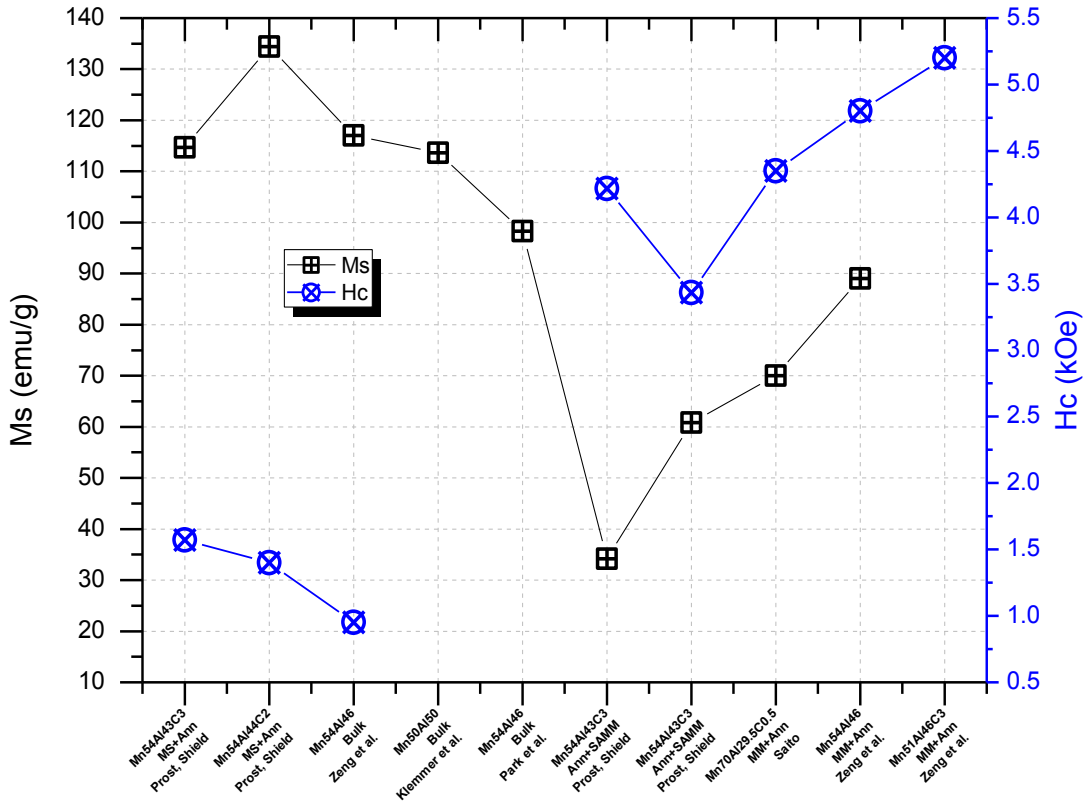

Figure 48 Magnetic properties of various samples of Mn-Al alloys with composition and processing displayed. To the left bulk samples, to the right mechanically milled samples; notice tradeoff between H_c and M_s.

In all the samples created for this study compare well with their respective literature counterparts (bulk processed material and mechanically milled material separately). And the tradeoff between Ms and Hc is typical for this system and is ubiquitous throughout the magnetic materials community.

Chapter 4

CONCLUSIONS

Manganese-aluminum ternary alloy permanent magnets have been successfully synthesized by arc-melting and subsequent melt-spinning. The effects of additions of carbon and boron have been explored carefully. The results have conclusively shown that the addition of boron has little direct effect on the formation of the FM τ-phase ($L1_0$). However, it does appear to promote the formation of equilibrium phases upon cooling from the melt, leaving less ε-phase to transform. It also reduces the stability of the τ-phase in favor of the equilibrium phases (βMn (A13) and γ_2 ($D8_{10}$)). Changes in the phase diagram due to small additions have been suggested. And, the intentional use of boron to decrease phase purity in favor of high coercivity has been suggested. Most interestingly a maximum value of 134 emu/g was measured for a ternary alloy of $Mn_{54}Al_{44}C_2$ which is the highest reported currently.

Post-processing techniques such as HEBM and SAMM are shown to increase the coercivities of the alloys. Maximum coercivities of 3.88 kOe and 4.22 kOe were observed for the HEBM samples and SAMM samples, respectively. However, both techniques for reducing the grain size inevitably amorphize the magnetic τ-phase which drives down the M_s inherently. And, it is clear that the SAMM samples exhibit similar morphologies after 8 hours of milling which indicates re-welding of grains. To avoid this, different processing procedures concerning type and amount of surfactant will be attempted.

References

[1] B.D. Cullity and C.D. Graham, *Introduction to Magnetic Materials*, 2nd ed., L. Hanzo, Ed. Hoboken, United States of America: JOhn Wiley & Sons, Inc., 2009.

[2] A. Hernando, C. Gomez-Polo, M. El Ghannami, and A. Garcia Escorial, "Approach to saturation and magnetic properties of melt-spun Fe-Cu granular systems," *Journal of Magnetism and Magnetic Materials*, vol. 173, pp. 275-286, 1997.

[3] H Kono, "On the ferromagnetic phase in manganese-aluminum system," *Journal of the Physical Society of Japan*, vol. 13, no. 12, pp. 1444-1451, 1958.

[4] R. Skomski, "Phase formation in L10 magnets," *Journal of Applied Physics*, vol. 101, no. 09N517, pp. 1-3, May 2007.

[5] T. Klemmer, D. Hoydick, H. Okumura, B. Zhang, and W.A. Soffa, "Magnetic Hardening and Coercivity Mechanisms in L10 Ordered FePd Ferromagnets," *Scripta Metallurgica et Materialia*, vol. 33, pp. 1793-1805, 1995.

[6] A. J. J. Koch, P. Hokkeling, M. G. v. d. Steeg, and K. J. de Vos, "New Material for Permanent Magnets on a Base of Mn and Al," *Journal of Applied Physics*, vol. 31, no. 5, pp. 75S-77S, 1960.

[7] K.J. Kim, K. Sumiyama, and K. Suzuki, "Ferromagnetic a-Mn-type Mn-Al alloys produced by mechanical alloying," *Journal of Alloys and Compounds*, vol. 217, pp. 48-51, 1995.

[8] E. Fazakas, L.K. Varga, and F. Mazaleyrat, "Preparation of nanocrystalline Mn-Al-C

magnets by melt spinning and subsequent heat treatments," *Journal of Alloys and Compounds*, vol. 434-435, pp. 611-613, 2007.

[9] Y.J. Kim and J.H. Perepezko, "Formation of a metastable ferromagnetic t phase during containerless melt processing and rapid quenching in Mn-Al-C alloys," *Journal of Applied Physics*, vol. 71, no. 2, pp. 676-680, January 1992.

[10] P.C. Kuo, Y.D. Yao, W.R. Chen, and J.H. Huang, "Preparation and magnetical studies of Mn50Al50/Al bilayer films," *Journal of Applied Physics*, vol. 81, no. 8, pp. 5253-5255, April 1997.

[11] T. Saito, "Magnetic properties of Mn-Al system alloys produced by mechanical alloying," *Journal of Applied Physics*, vol. 93, no. 10, pp. 8686-8688, May 2003.

[12] T. Saito, "Magnetic properties of Mn-Al-C alloy powders produced by mechanical grinding," *Journal of Applied Physics*, vol. 97, pp. 10F304-1-3, May 2005.

[13] L. Pareti, F. Bolzoni, F. Leccabue, and A.E. Ermakov, "Magnetic anisotropy of MnAl and MnAlC permanent magnet materials," *Journal of Applied Physics*, vol. 59, no. 11, pp. 3824-3828, June 1986.

[14] D.C. Crew, P.G. McCormick, and R. Street, "MnAl and MnAlC permanent magnets produced by mechanical alloying," *Scripta Metallurgica et Materialia*, vol. 32, no. 3, pp. 315-318, 1995.

[15] Q. Zeng, I. Baker, and Z.C. Yan, "Nanostructured Mn-Al permanent magnets produced by

mechanical milling," *Journal of Applied Physics*, vol. 99, no. 08E902, pp. 1-3, 2006.

[16] Q. Zeng, I. Baker, J.B. Cui, and Z.C. Yan, "Structural and magnetic properties of nanostructured Mn–Al–C magnetic materials," *Journal of Magnetism and Magnetic Materials*, vol. 308, no. 2, pp. 214-226, 2007.

[17] Y.C. Yang, W.W. Ho, and C. Lin, "Neutron diffraction study of hard magnetic alloy MnAlC," *Journal of Applied Physics*, vol. 55, no. 6, pp. 2053-2054, March 1984.

[18] Z.W. Liu, C. Chen, Z.G. Zheng, B.H. Tan, and R.V. Ramajujan, "Phase transitions and hard magnetic properties for rapidly solidified MnAl alloys doped with C, B, and rare earth elements," *Journal of Material Science*, vol. 47, pp. 2333-2338, October 2011.

[19] T.B. Massalski, *Minary Alloy Phase Diagrams*, 2nd ed., H. Okamoto, P.R. Subramanian, and L. Kacprzak, Eds. Materials Park, OH, United States of America: ASM, 1990.

[20] W.H. Dreizler and A. Menth, "Transformation kinetics of the ferromagnetic alloy Mn-Al-C," *Magnetics, IEEE Transactions on*, vol. M, no. 3, pp. 534-536, 1979.

[21] T. Ohtani, N. Kato, S. Kojima, K. Kojima, Y. Sakamoto, I. Konno, M. Tsukahara, and T. Kubo, "Magnetic Properties of Mn-Al-C Permanent Magnet Alloys," *IEEE Transactions on Magnetics*, vol. MAG-13, no. 5, pp. 1328-1330, September 1977.

[22] J.J. Van Den Broek, H. Donkersloot, and G. Tendeloo, "Phase transformations in pure and carbon-doped Al45Mn55 alloys," *Acta Metallurgica*, vol. 27, no. 9, pp. 1497-1504, September 1979.

[23] C. Yanar, J.M.K. Wiezorek, V. Radmilovic, and W.A. Soffa, "Massive Transformation and the Formation of the Ferromagnetic L10 Phase in Manganese-Aluminum-Based Alloys," *Metallurgical and Materials Transactions A*, vol. 33A, pp. 2413-2423, August 2002.

[24] J.H. Park, Y.K. Hong, S. Bae, J.J. Lee, J. Jalli, G.S. Abo, N. Neveu, S.G. Kim, C.J. Choi, and J.G. Lee, "Saturation magnetization and crystalline anisotropy calculations for MnAl permanent magnet," *Journal of Applied Physics*, vol. 107, no. 09A731, pp. 1-3, 2010.

[25] J.I. Langford, "The Use of the Voigt Function in Determining Microstructural Properties from Diffraction Data by means of Pattern Decomposition," in *Proceedings of the international conference Accuracy in Powder Diffraction II*, Gaithersburg, MD, 1992, pp. 110-126, National Institute of Standards and Technology Special Publication 846.

[26] P.R. Sperry and M.H. Bankard, "Metallographic Technique for Alluninum Alloys," in *Metals Handbook*, T. Lyman, H. E. Boyer, and W. J. Carnes, Eds. Metals Park: American Society for Metals, 1973, pp. 120-129.

[27] F. Jimenez-Villacorta, J. Marion, T. Sepehrifar, M. Daniil, M. a. Willard, and L. H. Lewis, "Exchange anisotropy in the nanostructured MnAl system," *Applied Physics Letters*, vol. 100, no. 112408, pp. 1-3, 2012.